

Semi-empirical quantum optics for mid-infrared molecular nanophotonics

Cite as: *J. Chem. Phys.* **156**, 124110 (2022); <https://doi.org/10.1063/5.0075894>

Submitted: 19 October 2021 • Accepted: 04 March 2022 • Accepted Manuscript Online: 04 March 2022

• Published Online: 25 March 2022

 **Johan F. Triana, Mauricio Arias,  Jun Nishida, et al.**



View Online



Export Citation



CrossMark

ARTICLES YOU MAY BE INTERESTED IN

[Selection of representative structures from large biomolecular ensembles](#)

The Journal of Chemical Physics (2022); <https://doi.org/10.1063/5.0082444>

[Simulation of absorption spectra of molecular aggregates: A hierarchy of stochastic pure state approach](#)

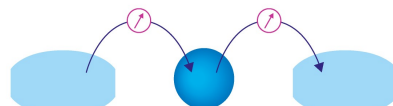
The Journal of Chemical Physics **156**, 124109 (2022); <https://doi.org/10.1063/5.0078435>

[Molecular vibrational polariton: Its dynamics and potentials in novel chemistry and quantum technology](#)

The Journal of Chemical Physics **155**, 050901 (2021); <https://doi.org/10.1063/5.0054896>

Webinar

Interfaces: how they make or break a nanodevice



March 29th – Register now

 **Zurich
Instruments**

Semi-empirical quantum optics for mid-infrared molecular nanophotonics

Cite as: *J. Chem. Phys.* **156**, 124110 (2022); doi: [10.1063/5.0075894](https://doi.org/10.1063/5.0075894)

Submitted: 19 October 2021 • Accepted: 4 March 2022 •

Published Online: 25 March 2022



View Online



Export Citation



CrossMark

Johan F. Triana,^{1,a)} Mauricio Arias,² Jun Nishida,³ Eric A. Muller,^{4,b)} Roland Wilcken,³ Samuel C. Johnson,³ Aldo Delgado,^{2,5} Markus B. Raschke,^{3,c)} and Felipe Herrera^{1,5,d)}

AFFILIATIONS

¹ Department of Physics, Universidad de Santiago de Chile, Av. Victor Jara, 3493 Santiago, Chile

² Departamento de Física, Facultad de Ciencias Físicas y Matemáticas, Universidad de Concepción, Concepción, Chile

³ Department of Physics and JILA, University of Colorado, Boulder, Colorado 80309, USA

⁴ Department of Chemistry, Colgate University, Hamilton, New York 13346, USA

⁵ ANID-Millennium Institute for Research in Optics, Concepción, Chile

Note: This paper is part of the JCP Special Topic on Advances in Modeling Plasmonic Systems.

^{a)}johan.triana@usach.cl

^{b)}emuller@colgate.edu

^{c)}markus.raschke@colorado.edu

^{d)}**Author to whom correspondence should be addressed:** felipe.herrera.u@usach.cl

ABSTRACT

Nanoscale infrared (IR) resonators with sub-diffraction limited mode volumes and open geometries have emerged as new platforms for implementing cavity quantum electrodynamics at room temperature. The use of IR nanoantennas and tip nanoprobes to study strong light–matter coupling of molecular vibrations with the vacuum field can be exploited for IR quantum control with nanometer spatial and femtosecond temporal resolution. In order to advance the development of molecule-based quantum nanophotonics in the mid-IR, we propose a generally applicable semi-empirical methodology based on quantum optics to describe light–matter interaction in systems driven by mid-IR femtosecond laser pulses. The theory is shown to reproduce recent experiments on the acceleration of the vibrational relaxation rate in infrared nanostructures. It also provides physical insights on the implementation of coherent phase rotations of the near-field using broadband nanotips. We then apply the quantum framework to develop general tip-design rules for the experimental manipulation of vibrational strong coupling and Fano interference effects in open infrared resonators. We finally propose the possibility of transferring the natural anharmonicity of molecular vibrational levels to the resonator near-field in the weak coupling regime to implement intensity-dependent phase shifts of the coupled system response with strong pulses and develop a vibrational chirping model to understand the effect. The semi-empirical quantum theory is equivalent to first-principles techniques based on Maxwell’s equations, but its lower computational cost suggests its use as a rapid design tool for the development of strongly coupled infrared nanophotonic hardware for applications ranging from quantum control of materials to quantum information processing.

Published under an exclusive license by AIP Publishing. <https://doi.org/10.1063/5.0075894>

I. INTRODUCTION

A wide range of natural and engineered material platforms have been used to study cavity quantum electrodynamics (QED¹) for applications in quantum sensing,² quantum communication,³ and quantum information processing.⁴ Under strong light–matter coupling, quantized excitations of the electromagnetic field in a cavity can reversibly exchange energy and coherence with material excitations. This coherent interaction competes with

radiative and non-radiative dissipative processes that naturally occur on the degrees of freedom of atoms,^{5–9} molecules,^{10,11} solid-state defects,¹² or superconducting qubits.³ For weaker coupling, the cavity field can accelerate the decay of material excitations and internal state coherences,¹³ an effect exploited in different cavity QED platforms for cooling,¹⁴ reservoir engineering,¹⁵ and enhanced imaging.¹⁶

While cavity QED has been studied with different quantum systems over a wide region of the electromagnetic spectrum—GHz

to UV, the strong coupling regime with infrared-active molecular vibrations in Fabry-Perot (FP) cavities has only recently attracted significant attention.^{17–24} Given the weak transition dipole moments of infrared molecular transitions and their low energies and long resonant wavelengths (~ 3 – 15 μm), strong coupling is achieved collectively with a macroscopic number of molecular dipoles in diffraction-limited FP resonators. In this collective coupling scenario, selected chemical reactions have been shown to proceed at different rates inside infrared resonators in comparison to free space,^{25–28} which suggests the possibility of using the electromagnetic vacuum field as a resource for chemical catalysis.^{29–31} In addition to controlled chemistry,³² strong coupling in infrared cavities could enable the development of novel mid-IR photon sources, infrared molecular qubits, and nonlinear optical elements that exploit the anharmonic potential of molecular vibrations.

Reducing the density of molecules and the mode volume of the mid-IR field can enable new experimental insights into the nature of the strong coupling regime with vibrational dipoles.³⁸ Nanoscale infrared resonator architectures have been developed for studies of cavity QED with ensembles of molecular vibrations^{33–36,39–43} or intersubband transitions.^{37,44} The densities of IR-active dipoles are significantly smaller in nanophotonic resonators in comparison with FP cavities. However, a strong coupling regime with an individual infrared dipole has yet to be demonstrated.

A range of theoretical approaches have been used previously to describe strong coupling in nanophotonics, varying in complexity from phenomenological coupled-oscillator fits to first-principles calculations using macroscopic QED.^{45,46} The latter approach is by construction consistent with Maxwell's equations and accurately describes the intrinsically non-Markovian character of the coupled light-matter dynamics of quantum emitters in optical nanostructures.^{47,48} However, the formalism is computationally expensive to implement due to the multiple evaluations of the electromagnetic Green's tensor needed to map the quantum dynamics of the coupled system over a range of frequencies, positions, and polarizations,^{47,49–53} which challenges its application to the rapid design and characterization of prototype nanophotonic quantum devices. On the other hand, simple classical oscillator models,^{54,55} while equivalent to quantum theory under some circumstances,^{32,56} fail to describe non-classical fields⁵⁷ and the strong coupling beyond the linear response.⁵⁸ Simple quantum mechanical models thus become a necessity for the development of infrared cavity QED on the nanoscale.

In this work, we propose a *semi-empirical* open quantum system approach to study cavity QED in infrared resonators driven by femtosecond pulses. The quantum state of the coupled light-matter system evolves according to a Markovian quantum master equation in the Lindblad form, whose coherent and dissipative parameters are obtained from independent experiments. Our quantum optics approach is shown to have predictive power that is equivalent to classical oscillator models under the appropriate conditions but can potentially offer new insights on genuine quantum phenomena in situations that are beyond the capabilities of classical models. In terms of computational complexity, our methodology is thus a compromise between a fully *ab initio* macroscopic QED approach and phenomenological classical coupled-oscillator models. The complexity of our methods can be systematically expanded to include the effect of multiple laser pulses, the dynamics of the probe

nanotips used for imaging and field manipulation, and the natural anharmonicity in the internal level spectrum of materials.

We validate our methodology by quantitatively reproducing previous tip nanoprobe IR-vibrational spectroscopy experiments.^{33,34} The theory is shown to match time-domain and frequency-domain observables of the coupled dipole-resonator systems under weak and strong coupling and provides straightforward insights into the dynamical role of probe nanotips on the manipulation of strong coupling and Fano interference effects (Sec. III). We then use the quantum formalism beyond linear response to predict novel phenomena enabled by IR-molecule picocavities, where classical models fail. This includes the prediction of a new type of anharmonic blockade effect, formulated in the collective single-mode approach, that results in a phase rotation of the coupled resonator field that scales nonlinearly with the input pulse power (Sec. IV). For molecular vibrations, we predict phase shifts of a few radians for a single femtosecond pulse that can produce population up to the second excited vibrational level. In contrast with other anharmonic blockade mechanisms in cavity QED, the proposed infrared nonlinearity does not rely on strong light-matter coupling,⁵⁹ optomechanical effects,⁶⁰ or long-range interactions between dipoles.⁶¹

II. CROSSOVER FROM WEAK TO STRONG COUPLING

Before describing the proposed quantum approach for infrared nanophotonics, let us first review basic cavity QED phenomenology relevant for this work. Figure 1(a) illustrates a molecular vibration dipole with fundamental frequency ω_v that couples to the near-field mode of an infrared resonator with frequency ω_a . The single-particle light-matter coupling strength is denoted by g . Vibrational dipoles in polyatomic molecules dissipate their energy into the coupled many-body vibrational manifold with an overall rate γ . The near-field undergoes non-radiative cavity loss through, e.g., Drude damping into the metal nanostructure at a rate κ_{nr} and radiative loss into the far-field at rate κ_r . The total photon loss rate is thus $\kappa = \kappa_{nr} + \kappa_r$. Spectroscopic observables of the coupled system depend on these parameters.

In general, a coupled light-matter system evolves with eigenfrequencies and decay rates that differ from the uncoupled case. This is shown in Fig. 1(b), where we plot the material ($T_{2\gamma}$) and photonic ($T_{2\kappa}$) dephasing times of coupled light-matter systems with different κ/γ ratios as a function of the cooperativity parameter $Ng^2/\kappa\gamma$, where N is the number of molecular dipoles in the system. In a simple description that ignores inhomogeneous broadening,^{56,62} a strongly coupled dipole-resonator system decays at a rate that is the average of the material and photonic rates. Such hybridization of timescales formally occurs for resonant coupling when $4\sqrt{N}g/|\kappa - \gamma| \geq 1$,^{54,55} where $|\kappa - \gamma| \neq 0$ is the decay mismatch. However, as Fig. 1(b) illustrates, timescale hybridization can, in principle, occur under conditions that would not be spectroscopically considered strong coupling. In this regime, we also expect the formation of polaritonic states that form a spectrally resolved doublet separated by the Rabi splitting $\Omega \equiv 2\sqrt{N}g$ under resonant conditions. Polariton formation occurs when Ω is greater than the individual linewidths κ and γ . Demanding that $\Omega \geq \{2\kappa, 2\gamma\}$ imposes the strong coupling condition

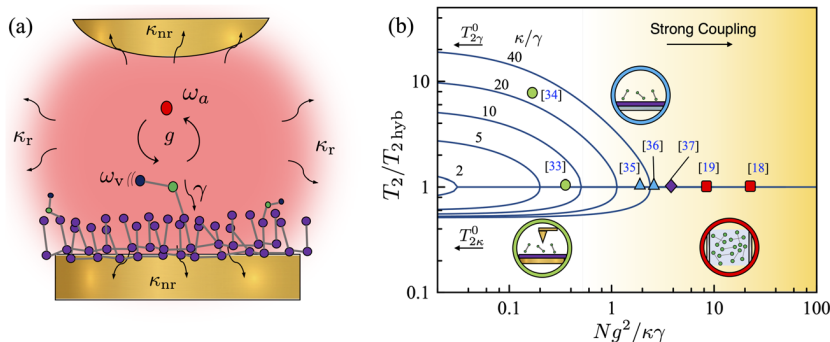


FIG. 1. Infrared nanocavity quantum electrodynamics. (a) A nanocavity confined infrared photon field resonant at frequency ω_a with radiative decay rate κ_r and non-radiative decay κ_{nr} coupled with a molecular vibration with absorption frequency ω_v and vibrational relaxation rate γ . The total photon decay rate is $\kappa = \kappa_r + \kappa_{nr}$. The cavity photon exchanges energy with the material quantum states at rate g . (b) Photonic ($T_{2\kappa}$) and material ($T_{2\gamma}$) dephasing times as a function of the cooperativity parameter $Ng^2/\kappa\gamma$. For small cooperativities (weak coupling), the photonic and material dephasing times are different when $\kappa \neq \gamma$. For cooperativities that exceed unity (strong coupling), a single hybrid dephasing time $T_{2\text{hyb}}$ is established. Selected infrared cavity implementations using tip-enhanced IR antenna resonators^{33,34} (green circles), planar nanocavities^{35,36} (blue triangles), intersubband quantum well heterostructures³⁷ (purple diamond), and liquid-phase Fabry-Perot microcavities^{18,19} (red squares) are given.

$$Ng^2/\kappa\gamma \geq 1. \quad (1)$$

In the weak coupling regime, Fig. 1(b) shows that the material dephasing time $T_{2\gamma}$ decreases with respect to its free space value $T_{2\gamma}^0 \equiv 2/\gamma$ as the cooperativity approaches the strong coupling region from the left. For resonant conditions, the dephasing time scales with the cooperativity as

$$T_{2\gamma} = \frac{T_{2\gamma}^0}{1 + 4Ng^2/\kappa\gamma}, \quad (2)$$

which is a signature of the Purcell effect.⁶² The reduction in $T_{2\gamma}$ is accompanied by an increase in the photon lifetime $T_{2\kappa}$ with respect to its free space value $T_{2\kappa}^0 \equiv 2/\kappa$ although for systems with $\kappa/\gamma \gg 1$, as expected for most open cavity systems, this change in the photon lifetime is only modest. The hybrid dephasing time $T_{2\text{hyb}}/2 \equiv (1/T_{2\kappa}^0 + 1/T_{2\gamma}^0)^{-1}$ is established for $Ng^2/\kappa\gamma \gg 1$. Although Fig. 1(b) describes a wide range of experimentally relevant scenarios, we note that natural sources of inhomogeneity in the material and photon system can result in significant deviations from the behavior described above.³² In the following sections, we further describe the light-matter coupling theory with molecular vibrations at the mid-infrared spectral range. The hybrid system under study is formed by gold nanoantennas coated with a thin polymer with carbonyl stretching modes that couple to the near-field of an antenna driven on resonance by a single femtosecond pulse. Such systems have been implemented experimentally in Refs. 33 and 34.

III. COUPLED TIP-RESONATOR-VIBRATION DYNAMICS IN THE LINEAR REGIME

A. Lindblad quantum master equation

We start by generalizing the scheme in Fig. 1(a) to treat an ensemble of N molecular vibrations with light-matter coupling at rate g_i of the i th molecular vibration with the resonator field.

In general, the uncoupled spectrum of the near-field is highly structured,⁵³ but for simplicity, we assume a single-mode resonator field with annihilation operator \hat{a} and resonance frequency ω_a . The total system Hamiltonian can be written as (we use $\hbar \equiv 1$ throughout)

$$\hat{\mathcal{H}}_N = \omega_a \hat{a}^\dagger \hat{a} + \sum_{i=1}^N \hat{T}_i + \hat{V}_i(q) + g_i \hat{d}_i(q) \otimes (\hat{a} + \hat{a}^\dagger), \quad (3)$$

where \hat{T}_i and $\hat{V}_i(q)$ are the nuclear kinetic energy and potential energy curve along the normal mode coordinate q in the i th molecule, respectively, and $\hat{d}_i(q)$ is a dimensionless electric dipole operator that depends parametrically on the vibrational coordinate q . The eigenstates $|\nu\rangle$ and eigenvalues E_ν for each of the single-molecule vibrational Hamiltonians $(\hat{T}_i + \hat{V}_i)$ are assumed to be known from free space IR spectroscopy with $\nu = 0, 1, 2, \dots$ being the vibrational quantum number.

We model driving and dissipation in the evolution of the reduced density matrix of the coupled molecule-resonator system $\hat{\rho}_S(t)$ with a quantum master equation of the Lindblad form,⁶³

$$\frac{d}{dt} \hat{\rho}_S = -i[\hat{\mathcal{H}}_N + \hat{H}_F(t), \hat{\rho}_S] + \mathcal{L}_\kappa[\hat{\rho}_S] + \mathcal{L}_{\gamma_C}[\hat{\rho}_S] + \mathcal{L}_{\gamma_L}[\hat{\rho}_S], \quad (4)$$

where $[\hat{A}, \hat{B}]$ denotes a commutator and $\mathcal{L}[\hat{\rho}_S]$ is a superoperator that describes dissipation. The system Hamiltonian $\hat{\mathcal{H}}_N$ is adapted from Eq. (3), and the driving term is given by

$$\hat{H}_F(t) = F_d(t) \left[\hat{a} e^{i\omega_d t} + \hat{a}^\dagger e^{-i\omega_d t} \right], \quad (5)$$

where $F_d(t)$ is proportional to the photon flux of the laser pulse. For dissipation, we consider photon decay at the overall rate κ and vibrational relaxation into a local reservoir at rate γ_L and into a collective

reservoir at rate γ_C . For specific expressions of the dissipators, see [Appendix A](#).

B. The vibrational Purcell effect

We first consider weak driving conditions ($|F_d|/\kappa \ll 1$). Far-field photons injected into the near-field can leak out on femtosecond time scales due to the short photon lifetimes of typical IR antenna resonators. Therefore, vibrational ladder climbing cannot occur over a pulse duration. Since only $v = 0$ and $v = 1$ levels can be probed, the local vibrational potential can be truncated to quadratic terms in q , i.e., $V_i(q) \approx \omega_v q^2/2$, and the dipole function $d(q)$ up to linear terms.^{64,65} We further ignore counter-rotating terms in Eq. (3) and the inhomogeneity in the vibrational frequencies and Rabi couplings.

From Eq. (4), we derive the following set of coupled equations for light and matter coherences:

$$\frac{d}{dt} \langle \hat{a} \rangle = -(i\omega_a + \kappa/2) \langle \hat{a} \rangle - i\sqrt{N}g \langle \hat{B}_0 \rangle - i\tilde{F}_d(t), \quad (6)$$

$$\frac{d}{dt} \langle \hat{B}_0 \rangle = -(i\omega_v + \gamma/2) \langle \hat{B}_0 \rangle - i\sqrt{N}g \langle \hat{a} \rangle, \quad (7)$$

where the material coherence is modeled as a collective oscillator $\hat{B}_0 \equiv \sum_i \hat{b}_i / \sqrt{N}$ with \hat{b}_i being a local vibrational mode operator. $\gamma \equiv N\gamma_C + \gamma_L$ and $\tilde{F}_d \equiv F_d(t) \exp[-i\omega_d t]$ with carrier frequency ω_d . Equations (6) and (7) correspond to driven coupled oscillators in the mean field and can be shown to be equivalent to the classical oscillator picture.³² For a single excitation pulse of arbitrary shape and frequency, exact analytical solutions for $\langle \hat{a}(t) \rangle$ and $\langle \hat{B}_0(t) \rangle$ are given in [Appendix B](#), which are valid both in the weak and strong coupling regimes and are consistent with previous work.⁶⁶

We test the predictions of Eqs. (6) and (7) by reprocessing experimental data from Ref. 34 on the dynamics of the near-field $E_{\text{nf}}(t) \propto \langle \hat{a}(t) \rangle$ for gold nanowire antennas coated with a thin film of poly(methyl-methacrylate) (PMMA) for its carbonyl (C=O) stretch mode vibrational oscillators under the influence of a single femtosecond IR pulse. We model the pulse with a Gaussian driving

term $F_d(t) = (F_0 / \sqrt{2\pi T}) \exp[-(t - t_0)^2 / 2T^2]$, where $T = 155$ fs is the pulse duration. $|F_0|^2$ is proportional to the photon flux per pulse injected to the resonator field. The pulse is centered at t_0 , and the system is initially in the absolute ground state (no photonic or material excitation). From the analysis in the following, we estimate the ratio $4\sqrt{N}g/\kappa - \gamma \approx 0.3$ (weak coupling) for these experiments.

The tip-enhanced antenna near-field detection scheme is illustrated in [Fig. 2\(a\)](#). The IR pulse drives the molecule-coupled resonator, and the coherently scattered IR near-field is measured interferometrically by heterodyne detection.⁶⁷ [Figure 2\(b\)](#) shows the experimental coherence $\text{Re}\langle \hat{a}(t) \rangle$ for $N \sim 10^3$ carbonyl oscillators per mode volume.³⁴ The antenna frequency ω_a is resonant with the carbonyl vibration frequency ω_v in the polymer. κ is obtained from the width of the far-field scattering spectrum of the antenna ($\kappa/2\pi = \text{FWHM}$). Carbonyl vibration frequencies and linewidths in PMMA can be found in the range $\omega_v = 1730-1745 \text{ cm}^{-1}$ and $\gamma/2\pi \sim 10-30 \text{ cm}^{-1}$.⁶⁷

In [Fig. 2\(c\)](#), we show the simulated vibrational coherence $\text{Re}\langle \hat{B}_0(t) \rangle$, obtained from Eqs. (6) and (7) with parameters calibrated with the data in [Fig. 2\(b\)](#). By setting the collective Rabi coupling to $\sqrt{N}g = 41 \text{ cm}^{-1}$, the free-induction decay (FID) of the molecular coherence is found to match the experimental dephasing time ($T_{2\gamma} = 347$ fs) within the measurement uncertainties.

The direct equivalence between the decay time of the collective oscillator coherence $\langle \hat{B}_0(t) \rangle$ and the resonator field $\langle \hat{a}(t) \rangle$ is demonstrated in [Appendix A](#). There, we show that long after the pulse is over ($t \gg t_0 + T$), the collective oscillator in a fully resonant scenario $\omega_a = \omega_v = \omega_d$ decays as

$$\langle \hat{B}_0(t) \rangle \approx \frac{\sqrt{N}g f_0}{\Gamma_g} e^{\tilde{\gamma}^2 T^2 / 4} e^{-i\omega_v t - \tilde{\gamma}(t-t_0)/2}, \quad (8)$$

where $\Gamma_g \equiv \text{Re}\{\sqrt{\Delta_\Gamma^2 - 4N\gamma^2}\}$, $\Delta_\Gamma = (\gamma - \kappa)/2$, and the coupled vibrational decay rate $\tilde{\gamma} = \gamma P_{\text{vib}}$, written in terms of the vibrational Purcell factor

$$P_{\text{vib}} = 1 + \frac{4N\gamma^2}{\kappa\gamma}. \quad (9)$$

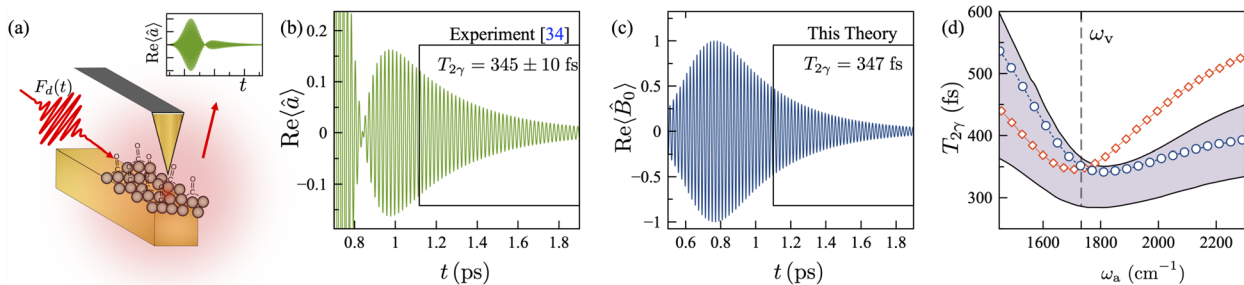


FIG. 2. Vibrational Purcell effect. (a) Field detection scheme for the PMMA-coated nanowire with the nanoscale local probing at the wire terminal. (b) Pulse-driven resonator field $\text{Re}\langle \hat{a}(t) \rangle$ measured in Ref. 34 for a resonant molecular vibration-antenna system ($\omega_v = \omega_a$). The measured lifetime of the FID signal is $T_{2\gamma} = 345 \pm 10$ fs (boxed region, inset). (c) Simulated collective molecular coherence $\text{Re}\langle \hat{B}_0(t) \rangle$ under equivalent conditions as in experiments with dephasing time $T_{2\gamma} = 347$ fs for $\sqrt{N}g = 41.5 \text{ cm}^{-1}$. (d) Simulated vibrational dephasing time as a function of the resonator frequency, assuming fixed coupling constant $\sqrt{N}g = 41.5 \text{ cm}^{-1}$ (red diamonds) and coupling constant scaling with the antenna resonance, $\sqrt{N}g \propto \omega_a$ (blue circles). The dashed line marks the vibrational frequency ω_v . In (b) and (c), the driving pulse is centered at $t_0 = 600$ fs and has a duration of $T = 155$ fs. We use $(\omega_v, \kappa/2\pi, \gamma/2\pi) = (1732, 519, 17) \text{ cm}^{-1}$.

P_{vib} quantifies the additional contribution to material relaxation that emerges from the coupling of the vibrational motion to the fast-decaying resonator field. In this Purcell-enhanced regime, the coupled vibrational dephasing time drops below its free space value of $T_{2y}^0 = 620$ fs in agreement with Eq. (2).

In Fig. 2(d), we compare the measured and simulated vibrational dephasing times T_{2y} as a function of the resonator frequency ω_a . The measured asymmetry with respect to the detuning from resonance, i.e., $\Delta_a \equiv \omega_a - \omega_v$, can be attributed to the strong frequency dependence of κ and g in nanoresonators.^{45,47,50} For comparison, an infrared cavity with frequency-independent κ and g would result in a symmetric Purcell factor as a function of detuning of the form $P_{\text{vib}}(\Delta_a) = 1 + Ng^2\Delta_\Gamma/\gamma(\Delta_a^2 + \Delta_\Gamma^2)$. On the other hand, partial agreement with experiments is obtained for red-detuned resonators when we assume the frequency-independent Rabi coupling $\sqrt{N}g$ to be 41 cm^{-1} . In this case, the asymmetry is not captured, and the Purcell factor is underestimated for antennas that are blue detuned from the vibrational resonance.

In order to capture the asymmetry observed in experiments [Fig. 2(d), shaded area], we extract the frequency-dependent decay rates $\kappa(\omega_a)$ from the scattering spectra of a series of gold infrared resonators (see Appendix A for details). Then $\sqrt{N}g$ is set for different values of ω_a to match the measured and simulated vibrational T_{2y} times for the resonators. Under the assumption that the molecule number N is only determined by the density of carbonyl bonds in the polymer film, we obtain a linear scaling of the single-molecule coupling $g \propto \omega_a$ to match the experimental dephasing times over the entire range of resonator frequencies studied. These scalings, in principle, can be derived with a macroscopic QED analysis,⁴⁵ but this is outside the scope of the semi-empirical approach adopted in this work. The modification of dephasing times T_{2y} is a result of the antenna–vibration coupling rate exceeding the intramolecular non-radiative relaxation κ_{nr} . The antenna acts as an external agent that modifies molecular IR emission, as Fig. 1(a) illustrates.

C. Nanotip control of the resonator phase

In Sec. III B, the nanotip only negligibly affects the molecule–antenna coupling itself and simply serves as a local probe of the near-field response.³⁴ We now relax this assumption by explicitly considering the relevant degrees of freedom of the tip in the quantum master equation in order to build physical insight on the conditions necessary for a nanotip to induce coherent phase transformations on the infrared near-field, as shown in recent experiments.³³

We start by modeling the electromagnetic field of the localized surface plasmon resonance at the tip apex with a bosonic operator \hat{c} at frequency ω_t . The tip couples directly to the antenna resonator field with coupling strength g_{at} and, in principle, can also couple directly to the molecular vibrations with a collective coupling strength $\sqrt{N}g_{\text{vt}}$. For simplicity, we assume that the tip field couples with the same number of vibrations N as the antenna field. The tip–antenna–vibration Hamiltonian can thus be written as $\hat{H} = \hat{H}_N + \hat{H}_T$, where the term \hat{H}_N is given by Eq. (3) and \hat{H}_T is given by

$$\hat{H}_T = \omega_t \hat{c}^\dagger \hat{c} + g_{\text{at}} (\hat{a}^\dagger \hat{c} + \hat{a} \hat{c}^\dagger) + \sqrt{N}g_{\text{vt}} (\hat{B}_0 \hat{c}^\dagger + \hat{B}_0^\dagger \hat{c}). \quad (10)$$

Figure 3(a) illustrates the tip–antenna–vibration system. Depending on the lateral tip position x , the phase front of a far-field pulse can be different at the tip apex relative to an antenna reference position due to a path length difference (retardation). Denoting this relative phase by $\Delta\phi = n_{\text{eff}} 2\pi x/\lambda_a$, where λ_a is the laser wavelength and n_{eff} is the refractive index of the medium, the coherent driving term in Eq. (5) now generalizes to

$$\hat{H}_F(t) = F_1 \phi_1(t) \hat{a} e^{i(\omega_1 t + \Delta\phi)} + F_2 \phi_2(t) e^{i\omega_2 t} \hat{c} + \text{H.c.}, \quad (11)$$

which separately describes driving of the resonator and the tip. “H.c.” stands for the Hermitian conjugate. The local pulse profiles are denoted by $\phi_i(t) = \exp[-(t - t_0)^2/2T_i^2]$, where $i = 1$ denotes the resonator and $i = 2$ denotes the tip. F_i is the peak field amplitude, and ω_i is the carrier frequency. Photon decay now also occurs due to the finite lifetime of the tip field at rate κ_t , which again includes both radiative and non-radiative contributions. For clarity, we have changed the notation from κ to κ_a for the photon decay rate of the antenna field.

By constructing a quantum master equation with the Hamiltonians in Eqs. (10) and (11), in Appendix C, we derive coupled mean field equations for $\langle \hat{a}(t) \rangle$, $\langle \hat{B}_0(t) \rangle$, and $\langle \hat{c}(t) \rangle$. In order to model the experiments in Ref. 33, we set $g_{\text{vt}} = 0$, $F_1 = F_2 = F$, and $\phi_1(t) = \phi_2(t) = \phi(t)$ and solve for the resonator field in the Fourier domain as $\langle \hat{a}(\omega) \rangle = \chi_T(\omega) \tilde{F}(\omega)$, where $\chi_T(\omega)$ is the coupled resonator response function and $\tilde{F}(\omega) \equiv F\phi(\omega)$ is the frequency-domain pulse amplitude. With the full analytical expression for $\chi_T(\omega)$ given in Appendix C, for the conditions relevant to Ref. 33, we obtain

$$\chi_T(\omega) \approx \frac{\chi_a(\omega) [e^{i\Delta\phi} + g_{\text{at}} \chi_t(\omega)]}{1 - \chi_a(\omega) [Ng_{\text{av}}^2 \chi_v(\omega) + g_{\text{at}}^2 \chi_t(\omega)]}, \quad (12)$$

where $\chi_a(\omega) \equiv (\omega - \omega_a - i\kappa_a/2)^{-1}$ is the response of the bare antenna, $\chi_v(\omega) = (\omega - \omega_v - iy/2)^{-1}$ is the bare vibrational response, and $\chi_t(\omega) = (\omega - \omega_t - i\kappa_t/2)^{-1}$ is the bare tip response. For clarity, we have changed the notation from g to g_{av} for the molecule–antenna–vibration coupling.

Figure 3(b) shows the measured imaginary part of $\chi_T(\omega)$ as a function of the relative phase $\Delta\phi$, reconstructed from data in Ref. 33. The line shape changes from absorptive to dispersive as the relative phase $\Delta\phi \propto x/\lambda_a$ increases. For $\Delta\phi \approx 0$, the response is purely absorptive and exhibits a Rabi splitting $\Omega \approx 46\text{ cm}^{-1}$ around the bare vibrational resonance in close agreement with the reported $\Omega = 47 \pm 5\text{ cm}^{-1}$ in Ref. 33 that corresponds to a population transfer of 115 fs or a coherence transfer of 230 fs. From the Rabi splitting, we estimate $\sqrt{N}g_{\text{av}} = 23\text{ cm}^{-1}$ and a ratio $4\sqrt{N}g_{\text{av}}/|\kappa_a - \gamma| \approx 1.6$, which fulfills the hybridization condition under resonance.

In Fig. 3(c), we plot the simulated response of the coupled resonator with a set of parameters extracted from the data in Fig. 3(b). The simulated phase rotation of the response is in qualitative agreement with experiments although further calibration work similar to the one carried out in Sec. III B would be needed to reproduce experimentally observed frequency shifts and spectral asymmetries observed in experiments [Fig. 3(b)] but not in the theory.

As a figure-of-merit for the phase rotation, we choose $\Phi \equiv \tan^{-1}(\text{Im}[\chi_T]/\text{Re}[\chi_T])$ at the vibrational frequency ω_v . In Fig. 3(d), we show the dependence of $\Phi(\omega_v)$ on the

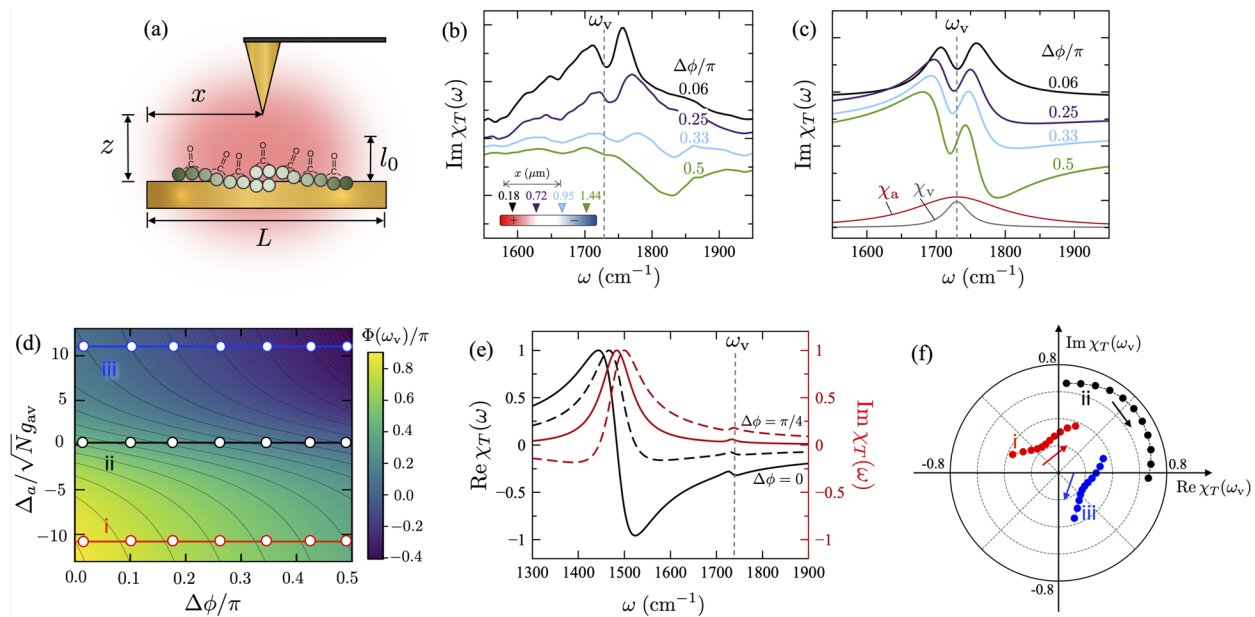


FIG. 3. Nanotip-induced phase rotation. (a) Molecular coupled IR antenna with vertical field confinement length l_0 , probed by the scanning nanotip. (b) Experimentally observed imaginary part of the coupled system response $\chi_T(\omega)$ with resonance wavelength $\lambda_a = 5.8 \mu\text{m}$ ($L = 1.75 \mu\text{m}$) for different values of the relative phase $\Delta\phi = 2\pi x/\lambda_a$. The vibrational resonance frequency is $\omega_v = 1730 \text{ cm}^{-1}$. (c) Simulated system response for selected values of $\Delta\phi$ with $(\gamma/2\pi, \omega_a, \kappa_a/2\pi, \sqrt{N}g_{av}, \kappa_t/2\pi, g_{at}) = (21, 1735, 80, 23, 800, 12) \text{ cm}^{-1}$. The bare vibrational and antenna responses $\chi_v(\omega)$ and $\chi_a(\omega)$ are shown for reference. (d) Antenna phase response at the vibrational resonance $\Phi(\omega_v)$ as a function of the input phase $\Delta\phi$ and the detuning-to-Rabi frequency ratio $\Delta_a/\sqrt{N}g_{av}$. Phase cuts i-iii at selected antenna detunings are highlighted. (e) Normalized real and imaginary parts of the total response $\chi_T(\omega)$ for input phases $\Delta\phi = 0$ (solid lines) and $\pi/4$ (dashed lines) for $\Delta_a = -11\sqrt{N}g_{av}$ (cut i in panel d). (f) Phasor diagram of the complex total response at the vibrational resonance $|\chi_T(\omega_v)|e^{i\Phi(\omega_v)}$ for cuts i-iii. Arrows show the direction of increasing $\Delta\phi$.

antenna–vibration detuning Δ_a and the input phase $\Delta\phi$. Frequency cuts at different detunings (cuts i-iii) show the predicted linear phase-to-phase relation at the fixed antenna frequency. The experiments in Ref. 33 correspond to $\Delta_a \approx 0$ (cut ii). In Fig. 3(e), we show the real and imaginary parts of the total response $\chi_T(\omega)$ for a red-detuned antenna field ($\omega_a = 1485 \text{ cm}^{-1}$) for $\Delta\phi = 0$ and $\Delta\phi = \pi/2$, highlighting the phase inversion at the vibrational resonance. In Fig. 3(f), we show a phasor diagram with sequences of the complex response at ω_v , i.e., $|\chi_T(\omega_v)|e^{i\Phi(\omega_v)}$, as the input phase $\Delta\phi$ is tuned from 0 to $\pi/2$. The predicted sequences correspond to different values of Δ_a .

Complementary to the Fourier-domain picture, the tip-induced phase rotations in Fig. 3 can be understood more generally from a time-domain perspective. For this, we exploit the separation of timescales $T_{2\kappa_t} \ll T_{2\kappa_a}$, where $T_{2\kappa_t} = 2/\kappa_t$, such that the tip field instantaneously adjusts to the dynamics of the antenna–vibration sub-system. We then adiabatically eliminate the tip variable $\langle \hat{c}(t) \rangle$ from the equations of motion and derive tip-renormalized evolution equations for $\langle \hat{a} \rangle$ and $\langle \hat{B}_0 \rangle$ of the form

$$\frac{d}{dt} \langle \hat{a} \rangle = -\left(i\omega'_a + \kappa'/2\right) \langle \hat{a} \rangle - g'_{av} \langle \hat{B}_0 \rangle + \mathcal{E}_a(t, \Delta\phi), \quad (13)$$

$$\frac{d}{dt} \langle \hat{B}_0 \rangle = -\left(i\omega'_v + \gamma'/2\right) \langle \hat{B}_0 \rangle - g'_{av} \langle \hat{a} \rangle + \mathcal{E}_v(t). \quad (14)$$

In comparison with Eqs. (6) and (7), the system frequencies and decay rates are now modified by the interaction with the tip. Expressions of the modified system frequencies ω'_v , decay rates (κ' and γ'), and light-matter coupling strength g'_{av} are given in Appendix C. The tip drives the resonator with a phase-dependent source $\mathcal{E}_a(t, \Delta\phi)$ and also the molecular vibrations through the source term $\mathcal{E}_v(t)$ when $g_{vt} \neq 0$. Full expressions for the tip-modified system frequencies, decay rates, and driving sources can be found in Appendix C.

We solve Eqs. (13) and (14) using Laplace transform techniques with $g_{vt} = 0$ to obtain an expression for the resonator field of the form

$$\langle \hat{a}(s) \rangle = \zeta e^{i\theta} \times \frac{(s + \gamma'/2 + i\omega'_v)}{p(s)} F(s), \quad (15)$$

where the polynomial $p(s) \equiv s^2 - s(i\omega'_c + \kappa'/2)(\gamma'/2 + i\omega'_v) + g'^2_{av}$ encodes the coupled system eigenfrequencies. $F(s)$ is the Laplace transform of the driving pulse. This expression shows that the resonator field is modulated by the stationary complex amplitude $Z = g'_{at} - ie^{i\Delta\phi} \equiv \zeta e^{i\theta}$, where $g'_{at} \approx -2g_{at}/\kappa_t$ is a dimensionless tip–antenna coupling parameter. For $|g'_{at}| \ll 1$, the coupled resonator response is rotated by $\theta \approx \Delta\phi - \pi/2$ ($g'_{at} = -0.03$ in Fig. 3).

By inverting Eq. (15) back to the time domain, the influence of the tip can be understood quantum mechanically as the time-independent phase-space transformation,

$$\hat{a}(t) \rightarrow \zeta e^{i\theta\hat{a}^\dagger\hat{a}} \hat{a}(t) e^{-i\theta\hat{a}^\dagger\hat{a}}, \quad (16)$$

which is a basic transformation in optical quantum information processing.⁶⁸

To summarize this section, we show that coherent field retardation effects observed in tip-antenna experiments can be simply encoded into the system Hamiltonian as relative phases between input driving fields [see Eq. (11)], thus facilitating a rapid analysis of tip-induced interference effects in comparison with a full vectorial electromagnetic field simulation.⁶⁹ The equations of motion obtained from the Lindblad quantum master equation admit Fourier-domain solutions that highlight the role of destructive and constructive interferences between the tip and antenna fields in the complex response of the coupled system [see Eq. (12)]. In comparison with our previous classical treatment of the coupled tip-antenna-vibration response in Ref. 33, the quantum optics approach removes the ambiguities in the definition of the uncoupled mode frequencies, thus facilitating the analysis of the coupled spectra. The quantum approach also predicts changes in both the phase and amplitude of the coupled response at the vibrational frequency ω_v (see Fig. 3(f)], which are not predicted classically.

The quantum picture shows that in a broadband limit where tip-localized photons decay much faster than in the near-field of the antenna resonator, reduced evolution equations for the antenna-vibration system can be derived such that its parameters depend explicitly on the tip-antenna coupling strength g_{at} , which is ultimately given by the overlap between the corresponding evanescent fields.⁷⁰ Coherent tip-induced phase-space rotations of the infrared near-field [see Eq. (16)] can thus be quantitatively studied as a function of design parameters such as quality factors, resonance frequencies, and field profiles. We expect this to

accelerate the development of mid-infrared quantum information devices. In what follows, we further explore the reach of the proposed quantum optics formalism beyond what has been currently done in experiments.

D. Tip-induced modulation of strong coupling

In addition to modifying the phase of the near-field by varying the lateral position x relative to the resonator surface, nanotips can also contribute to the crossover from weak to strong coupling as the vertical position z is tuned. Local modulation of strong coupling has been demonstrated with quantum dot emitters in optical nanoresonators^{71,72} but has yet to be implemented with infrared nanostructures. In order to theoretically study these effects, we now generalize the analysis in Sec. III C to allow for a more active role of the tip nanoprobe in the light-matter interaction process, beyond just probing the vibration-antenna coupling dynamics. Since the tip motion is essentially frozen over the relevant spectroscopic timescales, its position (x, z) can be mapped to stationary magnitudes of the tip-antenna coupling g_{at} and tip-vibration couplings g_{vt} as well as the input phase $\Delta\phi$. In order to focus on the interference between the tip-vibration and antenna-vibration couplings, throughout this section, we set $\Delta\phi = 0$.

In Fig. 4(a) we show the response of the coupled antenna-vibration system with Rabi splitting $\Omega \approx 46 \text{ cm}^{-1}$, probed by a broadband tip ($\kappa_t \gg g_{at}$) that is not directly coupled to vibrations [see also Fig. 3(c)]. For such a nanoprobe, we predict that by increasing the tip-vibration coupling strength $\sqrt{N}g_{vt}$ beyond the antenna and vibrational linewidths κ_a (80 cm^{-1}) and γ (21 cm^{-1}), for instance, by bringing the tip closer to the molecular layer, the Rabi splitting in the response does not increase but actually disappears. In this case, the broadband tip simply acts as an additional photonic bath for the molecules, effectively broadening the vibrational resonance through the Purcell effect discussed in Sec. III B when the tip-vibration coupling is large enough.

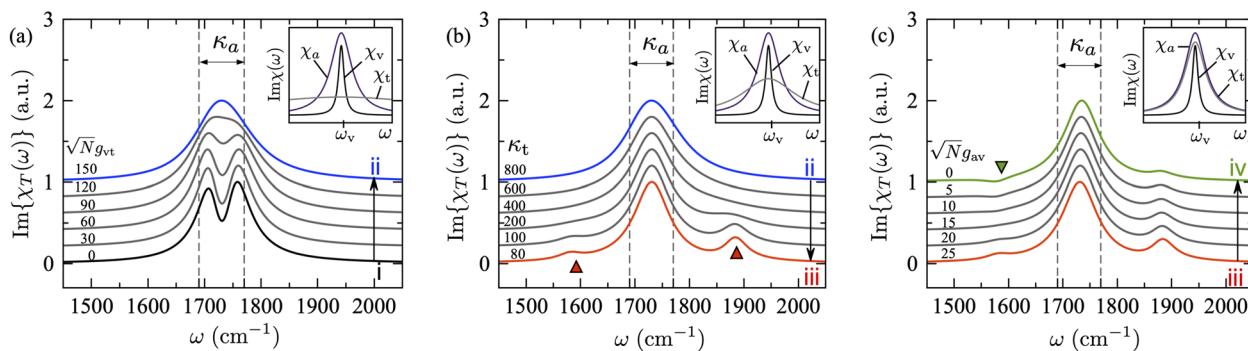


FIG. 4. Tip-antenna interaction and strong coupling. (a) Absorptive response of a fully resonant coupled antenna-vibration-tip system near the vibration frequency $\omega_v = 1730 \text{ cm}^{-1}$. Curves show the progression from a Rabi doublet with $\sqrt{N}g_{av} = 25 \text{ cm}^{-1}$ and vanishing tip-vibration coupling (i) to the simultaneous coupling with a very broad tip with $g_{vt} = 150 \text{ cm}^{-1}$ (ii). Vertical dashed lines indicate the bare antenna linewidth $\kappa_a/2\pi = 80 \text{ cm}^{-1}$. (b) Progression of the response for a decreasing tip linewidth from $\kappa_t/2\pi = 800 \text{ cm}^{-1}$ (ii) to $\kappa_t/2\pi = 80 \text{ cm}^{-1}$ (iii); all other parameters are kept constant. The emergence of a Rabi doublet at $\omega_v \pm g_{vt}$ is highlighted with triangles. (c) Progression as the antenna-vibration coupling decreases from $\sqrt{N}g_{av} = 25 \text{ cm}^{-1}$ (iii) to zero (iv). Fano interference at the lower Rabi peak is highlighted with a triangle. In all panels, the tip-antenna interaction is set to $g_{at} = 12 \text{ cm}^{-1}$, the relative tip-antenna phase is $\Delta\phi = 0$, and the insets show representative bare responses of the antenna χ_a , the tip χ_t , and the molecular vibration χ_v ($\gamma/2\pi = 21 \text{ cm}^{-1}$).

In Fig. 4(b), we show that a Rabi splitting can be recovered if the tip lifetime increases, while keeping g_{vt} and all other parameters constant. For κ_t comparable to κ_a , the separation of timescales used in Sec. III C does not apply. For large enough $\sqrt{N}g_{vt}$, the coupled antenna response consists of one center resonant feature at $\omega_a = \omega_v$ of width κ_a and two Rabi sidebands symmetrically located around the vibrational resonance at $\omega = \omega_v \pm \sqrt{N}g_{vt}$, which is the Fourier-domain signature of strong coupling ($Ng_{vt}^2/\kappa_t\gamma = 13.4$). Note that while the contribution of the bare antenna–vibration coupling to the Rabi splitting is negligible for the chosen parameters ($g_{av}/g_{vt} = 0.17$), the strong tip–vibration coupling maps into the observable $\langle \hat{a}(\omega) \rangle$ due to the finite tip–antenna coupling g_{at} .

As a third case study of the predicted linear response of the tip–antenna–vibration system, we show in Fig. 4(c) that the line shape of the Rabi split sidebands can be modified due to destructive and constructive Fano interference between overlapping response functions. In particular, the lower Rabi sideband has an absorption dip at $\omega_v - \Omega_{vt}/2$, where $\Omega_{vt} \equiv \sqrt{N}g_{vt}/2$ is the tip-induced splitting (300 cm^{-1}). We can understand this interference effect analytically, starting from a complete expression of the Fourier response of the resonator field of the form $\chi_T(\omega) = \chi_1 + \chi_2 + \chi_3 + \chi_4$, where the definition of the individual contributions is given in Eq. (C7) of Appendix C. For $g_{vt} = 0$, the full expression of the response reduces to Eq. (12) as a special case. The graphical analysis of the individual response terms is also given in Appendix C.

For the Fano line shape in Fig. 4(c) (curve iv), we turn off the antenna–vibration coupling ($g_{av} = 0$) and set $\kappa_a = \kappa_t = \kappa$ without losing generality. In this fully resonant scenario ($\omega_v = \omega_a = \omega_t$), we can approximately write the absorptive response of the coupled resonator at the frequencies of the lower and upper sidebands $\omega_{\pm} \equiv \omega_v \pm \Omega_{vt}/2$ as

$$\text{Im}\chi_T(\omega_{\pm}) \approx \frac{1}{\sqrt{N}g_{vt}} \left[\frac{\kappa/2}{\sqrt{N}g_{vt}} \pm \frac{g_{at}}{\kappa/2} \right], \quad (17)$$

showing destructive interference of the tip–vibration and tip–antenna responses at the lower sideband ω_- and constructive interference at the upper sideband ω_+ .

These results illustrate one of the key strengths of the semi-empirical Markovian quantum master equation approach: seemingly different quantum phenomena, such as the Purcell effect, Rabi splitting, and Fano interference, all emerge naturally from the same equations of motion in different parameter regimes. The quantum mechanical equations admit transparent analytical solutions for the system response that can be exploited for analyzing different experimental scenarios. In particular, theory suggests that in order to explore the fundamental connection between Rabi splitting and Fano interference with molecular vibrations, novel nanotip designs with narrow-band plasmonic resonances in the mid-infrared should be engineered.

IV. ANHARMONIC BLOCKADE EFFECT FOR STRONG DRIVING PULSES

After comparing the predictions of the Lindblad theory with linear response experiments on resonator–molecule systems in weak coupling²⁴ and strong coupling,²³ we now explore what the formalism predicts under strong driving conditions, motivated by search

of unconventional infrared signals that are sensitive to the spectral anharmonicity of molecular or material vibrations. In quantum optics, the ability to implement nonlinear optical transformations on the electromagnetic field that are relevant in quantum metrology depends on the anharmonicity of the system energy levels.⁷³ Such anharmonicities can occur, for example, due to strong light–matter coupling with individual dipoles,⁵⁹ via optomechanical interactions,⁶⁰ or due to long-range interactions between material dipoles.⁶¹ The vibrational levels of individual molecules have an intrinsic anharmonicity that is well understood in free space^{74–76} and has been recently studied in Fabry–Perot infrared cavities under strong coupling.^{23,24,77,78}

In Fig. 5(a), we illustrate the input–output scheme describing the phase evolution of the driven infrared near-field in a coupled vibration–resonator system. Relative to the phase of the driving pulse, the scattered pulsed field in the Fourier domain has a phase response of the form $\Delta\Phi(\omega) = \Delta\Phi_L(\omega) + \Delta\Phi_{NL}(\omega)$, where $\Delta\Phi_L$ is a trivial intensity-independent linear shift introduced by a tip nanoprobe and $\Delta\Phi_{NL}$ is a nonlinear contribution to the phase shift that depends on the driving pulse intensity. In this section, we propose a scheme to transfer the natural anharmonicity of vibrational energy levels to the phase response of the coupled system under conditions of strong pulse driving and weak vibration–resonator coupling (low cooperativity). We develop an approximate theoretical model based on the Lindblad quantum master equation to obtain the dependence of the nonlinear phase shift $\Delta\Phi_{NL}$ with the nominal pulse power and the degree of vibrational anharmonicity. While our analysis focuses on a collection of N molecular vibrations, the theory may also be applicable to describe other physical systems with anharmonic infrared and THz dipoles such as inter-subband quantum well transitions³⁷ and confined phonons in polar nanocrystals.⁷⁹

A. Vibrational anharmonicity model

The simplest anharmonicity model for a chemical bond relates to the expansion of the Born–Oppenheimer (BO) potential $V(q - q_e) = \sum_k \alpha_k (q - q_e)^k$ beyond second order around the equilibrium bond length q_e . Quartic nonlinearities ($k = 4$) give a sufficient description of spectral anharmonicities in vibrational modes with parity-symmetric BO potentials near equilibrium⁸⁰ and have been studied in the context of vibrational strong coupling spectroscopy in Fabry–Perot resonators.⁷⁷ This nonlinearity decreases the energy spacing between subsequent vibrational levels. In particular, the energy gap between the $v = 1$ and $v = 2$ levels is lower than the fundamental frequency ω_v by the anharmonic parameter Δ_{21} . The latter typically varies in the range $10\text{--}40 \text{ cm}^{-1}$ for polyatomic molecules.^{24,81,82} Minimal models for quartic nonlinearities have been used extensively in nonlinear IR spectroscopy.^{74–76} In their simplest form, the vibrational Hamiltonian for a single mode can be written in terms of harmonic oscillator variables \hat{b}_i in the Kerr form⁷⁴

$$\hat{T}_i + \hat{V}_i(q) \approx \omega_v \hat{b}_i^\dagger \hat{b}_i - U \hat{b}_i^\dagger \hat{b}_i^\dagger \hat{b}_i \hat{b}_i, \quad (18)$$

with $U = |\Delta_{21}|/2$. More general molecular anharmonicities that break parity have also been studied in the context of molecular cavity QED.^{24,64,65}

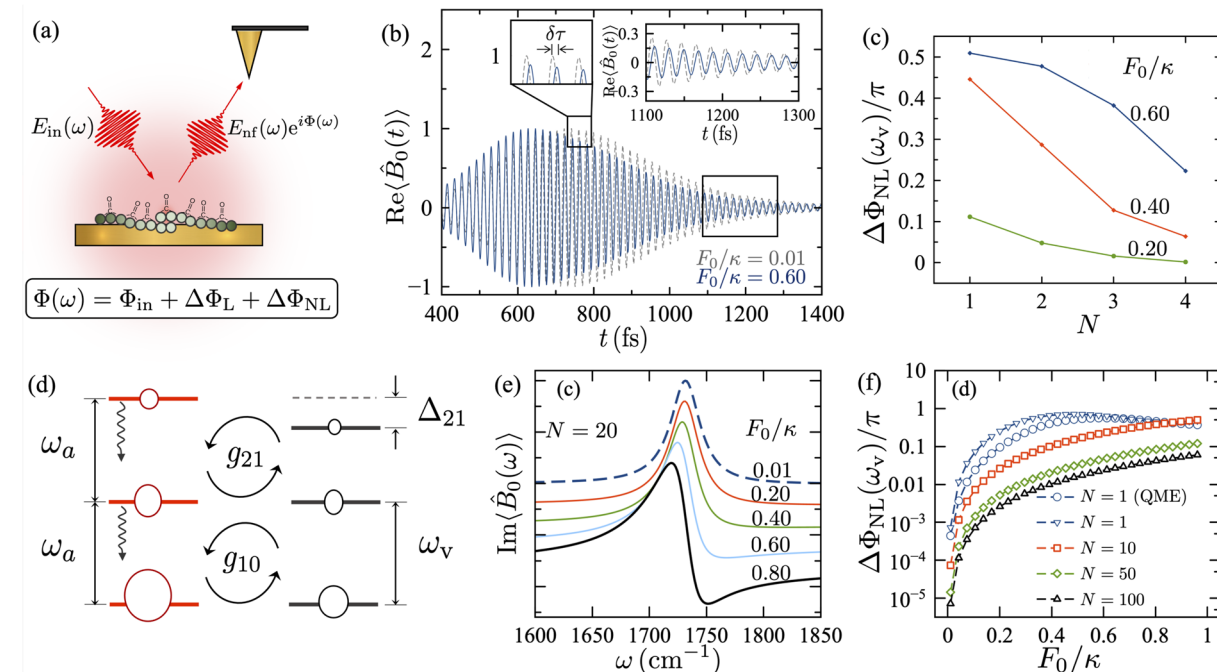


FIG. 5. Power-dependent phase rotation of the vibrational coherence. (a) Schematic picture of coherently scattered fields in molecule-coupled resonators. The output phase contains the driving phase Φ_{in} as well as linear and nonlinear phase shifts, $\Delta\Phi_L$ and $\Delta\Phi_{NL}$. (b) Evolution of the collective coherence $\text{Re}\{\hat{B}_0(t)\}$ for $N = 3$ anharmonic vibrations ($U = 20 \text{ cm}^{-1}$) subject to a single 155 fs pulse centered at 600 fs with driving strength parameters $F_0/\kappa = 0.6$ (solid line) and $F_0/\kappa = 0.01$ (dashed line). The delay $\delta\tau$ between the weak and strong field responses is highlighted. The inset shows a magnified view of the FID signal after the pulse is over (boxed region). (c) Nonlinear phase $\Delta\Phi_{NL}$ at bare resonance ($\omega_v = 1732 \text{ cm}^{-1}$) as a function of the molecule number N , obtained from exact solutions of the quantum master equation. Curves are shown for different values of F_0/κ . (d) Level scheme for resonant coupling between the antenna photon levels with anharmonic vibrations in the presence of a strong pulse. The ground and first excited levels exchange coherence and population resonantly, but the transition from the first to the second vibrational level is detuned from the antenna by $\Delta_{21} = 2U$. Level populations at the pulse maximum are represented as circles of different sizes. g_{10} and g_{21} denote state-dependent Rabi frequencies. (e) Imaginary part of the FID signal in the frequency domain for anharmonic oscillators with $\Delta_{21} = 40 \text{ cm}^{-1}$, obtained from the nonlinear chirping model. Curves are labeled by the ratio F_0/κ . (f) Nonlinear phase $\Delta\Phi(\omega_v)$ as a function of the ratio F_0/κ , as predicted by the nonlinear chirping model. Curves are shown for different molecule numbers N . Exact results from the quantum master equation for $N = 1$ are also shown for comparison. We set $\omega_v = \omega_a = \omega_d$ with other parameters as in Fig. 2.

B. Anharmonic blockade effect for strong pulsed excitation

We can simulate the coupled light-matter dynamics of anharmonic vibrations coupled to an infrared resonator by solving the quantum master equation in Eq. (4) with the local anharmonic vibrational Hamiltonian in Eq. (18) for a system of N molecules. The single-molecule Rabi frequency g , the local vibrational relaxation rate γ_L , and the cavity decay rate κ are set to be the same as in Fig. 2, i.e., the system is in weak coupling. For a driving strength parameter $F_0/\kappa \gtrsim 0.1$, we numerically compute the evolution of the collective coherence $\langle \hat{B}_0 \rangle = \sum_i \langle \hat{b}_i \rangle / \sqrt{N}$ by integrating the quantum master equation in a local vibrational basis up to $N = 4$. An exact integration of the quantum master equation for larger ensembles is computationally challenging, given the exponential scaling of the density matrix with the size of the basis set.

In Fig. 5(b), we plot the evolution of $\text{Re}(\hat{B}_0)$ for $N = 3$ and $F_0/\kappa = 0.6$, obtained as described above (solid line). We also show the response of a coupled system driven by a pulse that has the same normalized temporal profile ($t_0 = 600$ fs and $T = 155$ fs) but is much weaker ($F_0/\kappa = 0.01$, linear response). Resonant coupling and

driving is assumed ($\omega_v = \omega_a = \omega_d$), and the single-molecule nonlinearity parameter is $U = 20 \text{ cm}^{-1}$. The strongly driven signal develops a time delay $\delta\tau$ of a fraction of a cycle relative to weak driving (inset). This delay builds up gradually while the pulse is on and remains constant after the pulse is over. The vibrational decay time (T_{2y}) does not depend on the pulse strength.

From the complex time-domain signal $\langle \hat{B}_0(t) \rangle$, we compute the phase spectrum $\phi(\omega)$ in the Fourier domain and evaluate it at ω_v . We repeat for weak and strong driving conditions to get the nonlinear phase shift $\Delta\Phi_{\text{NL}}(\omega_v) = \phi_{\text{strong}}(\omega_v) - \phi_{\text{weak}}(\omega_v)$, where ϕ_{strong} is the signal phase under strong driving and ϕ_{weak} is the phase for the same coupled system subject to a weak reference pulse. In Fig. 5(c), we show the finite-size scaling of the nonlinear phase $\Delta\Phi_{\text{NL}}(\omega_v)$ with N for different driving strengths. The results highlight the main qualitative physics of the problem: (i) For a fixed molecule number and photon lifetime, the phase nonlinearity increases with pulse power. This is expected since the deviation from a pure harmonic oscillator becomes relevant when the system is excited to higher vibrational levels, which requires higher pulse intensities. (ii) For a given pulse strength, the phase nonlinearity decreases with the

increasing particle number. This excitation dilution effect has been studied extensively for ensembles of two-level systems⁸³ and more recently for multi-level systems.⁸⁴

We propose a vibrational chirping mechanism to understand the predicted nonlinear phase shift. Figure 5(d) illustrates a representative population distribution in the ground and first two excited levels of the photon field and the molecular vibrations at the peak amplitude of a strong driving pulse. For the strong field response in Fig. 5(b), the photonic and vibrational ground states are significantly depleted (see population evolution in Fig. 7 in Appendix D). For resonant coupling ($\omega_0 = \omega_v$), population and coherence transfer between the light–matter states $|n = 0\rangle|v = 1\rangle$ and $|n = 1\rangle|v = 0\rangle$ occurs rapidly and resonantly at the Rabi frequency g_{10} , proportional to the fundamental transition dipole $\langle v = 1|\hat{d}|v = 0\rangle$. Since the pulse also populates the two-photon state $|n = 2\rangle$, population and coherence exchange can occur between the states $|n = 2\rangle|v = 1\rangle$ and $|n = 1\rangle|v = 2\rangle$ at the rate g_{21} , proportional to the excited transition dipole $\langle v = 2|\hat{d}|v = 1\rangle$. However, this exchange is not resonant due to the anharmonic shift Δ_{21} of the $v = 2$ vibrational level. The excited photon field thus becomes *transiently* blue detuned from the $v = 2 \rightarrow v = 1$ transition. This transient detuning introduces a delay $\delta\tau$ in the response of the coupled vibration–resonator system, relative to a weak-pulse scenario in which no two-photon state is produced. Since the detuning disappears immediately after the pulse is over ($T_{2\kappa} \ll T$), the post-pulse delay is stationary and can be measured interferometrically.

C. Modeling the power-dependent phase rotation

As we mention above, obtaining converged solutions of the Lindblad master equation for large N is computationally hard. We therefore develop an approximate model that can qualitatively capture the dependence with the pump power and particle number of the nonlinear phase $\Delta\Phi_{\text{NL}}$ shown by the finite-size analysis in Figs. 5(b) and 5(c). The justification of the model is given in Appendix D, starting from equations of motion for the local vibrational coherences $\langle \hat{b}_i \rangle$. The model reduces to a closed nonlinear system of equations for the resonator coherence $\langle \hat{a} \rangle$ and the collective vibrational coherence $\langle \hat{B}_0 \rangle$. The evolution of $\langle \hat{a} \rangle$ is again governed by Eq. (6), but the evolution of $\langle \hat{B}_0 \rangle$ is now given by

$$\frac{d}{dt}\langle \hat{B}_0 \rangle = -(\gamma/2 + i[\omega_v - 2(U/N)|\langle \hat{B}_0 \rangle|^2])\langle \hat{B}_0 \rangle - i\sqrt{N}g\langle \hat{a} \rangle, \quad (19)$$

which differs from the weak driving evolution in Eq. (7) by the emergence of an effective vibrational chirp term, i.e., $\omega_v(t) = \omega_v - 2U|\langle \hat{B}_0(t) \rangle|^2/N$. The chirping effect captures the effective detuning of the quantized field from transitions between higher vibrational levels described above. The $1/N$ scaling of the chirp term captures the excitation dilution effect.

In Fig. 5(e), we use this vibrational chirping model to show that the time delay $\delta\tau$ in the system response can also change the Fourier response from absorptive to dispersive as a function of the pulse power ($N = 20$). This is reminiscent of the tip-induced phase-space rotation described earlier in linear response (Sec. III C), but now, the effect is due to molecular anharmonicity. We show in Fig. 5(f) the scaling of the nonlinear phase shift $\Delta\Phi_{\text{NL}}(\omega_v)$ with the driving strength parameter F_0/κ also within the chirping

model. Large phase shifts of order 0.1π are predicted for driving strengths that are comparable to the photon decay rate ($F_0 \sim \kappa$) using mesoscopic molecular ensembles ($N \lesssim 100$). These proof-of-concept results suggest the possibility of implementing nonlinear phase switches based on natural vibrational anharmonicities with currently available mid-infrared resonator architectures,³⁴ provided that high excitation densities can be sustained.

V. DISCUSSION AND CONCLUSION

In this work, we propose a semi-empirical theoretical methodology based on a Markovian quantum optics model for studying mid-infrared molecular nanophotonic devices. The method is *modular* in the sense that the Hamiltonians and super-operators respectively, that the coherent and dissipative evolution of bare vibrational and photonic variables, can be independently parameterized from spectroscopic measurements of the uncoupled subsystems. By interferometrically measuring the photon lifetime in the mid-IR near-field of an infrared antenna as a function of its resonance frequency, the uncertainty of the procedure for calibrating the light–matter coupling parameter of an antenna–vibration system can be kept below the vibrational linewidth ($\sim 10 \text{ cm}^{-1}$), allowing for theoretical predictions on the dynamics of the coupled light–matter system with a few-femtosecond precision, which is comparable with fully *ab initio* modeling based on macroscopic QED,^{45,50} but at a lower computational cost. This theoretical accuracy is desirable for the development of quantum nanophotonic devices that exploit natural phenomena in molecular materials in the mid-IR.

We used the proposed quantum optics approach in Secs. III B and III C to reinterpret recent nanoprobe spectroscopy measurements in weak coupling³⁴ and at the onset of strong coupling.³³ The experiments were originally interpreted using classical oscillator models. Good quantitative and qualitative agreement is shown between the classical and quantum models. Recent classical electrodynamics simulations of plasmonic nanocrystal dimers predict time-domain optical signals that are analog to the infrared response discussed in Sec. III B,⁸⁵ further emphasizing the known connection between quantum and classical modeling of linear spectroscopy.³² We then used quantum theory in Sec. III D to understand general design rules that would allow tip probes to actively manipulate the observe Rabi splittings and Fano interferences that can occur in the frequency response of coupled antenna–vibration systems. This analysis should stimulate the implementation of novel tip architectures with narrow-band plasmonic resonances that provide strong field confinements in the mid-infrared regime.⁸⁶

Finally, in Sec. IV, we studied novel infrared nonlinear effects that can be expected under strong pulsed excitation. For strong pulses that can induce population in the $v = 2$ excited vibrational level of the molecular ensemble, the phase response of a weakly coupled antenna–vibration system acquires a measurable shift that scales nonlinearly with the pulse power. This intensity-dependent phase shift is transferred to the infrared field from the natural anharmonicity of the excited vibrational levels. By solving the underlying quantum master equation in the basis of material and photonic degrees of freedom, we trace the origin of the nonlinearity to a transient chirping effect in which the driven resonator field becomes blue detuned with respect to the $v = 1 \rightarrow v = 2$ transition when both the

laser and the resonator are tuned to the fundamental vibrational resonance $\nu = 0 \rightarrow \nu = 1$. This new type of vibrational blockade effect is fundamentally different from other blockade mechanism in cavity QED that relies on strong coupling,⁵⁹ optomechanical couplings,⁶⁰ or long-range interactions between material dipoles⁶¹ and is proof-of-principle for the implementation of optical phase gates in the mid-IR in near-future experiments.

In summary, we implement a semi-empirical quantum optics framework for the quantitative and qualitative analysis of mid-infrared nanophotonic devices that exploit the coupling of near-field photons with localized vibrations in organic materials. By comparing with state-of-the-art experiments, we validate the predictions of the theory and demonstrate the feasibility of implementing classical linear and nonlinear phase operations on the infrared near-field, which represent the foundations for further theoretical and experimental work on quantum state preparation and control in the mid-infrared. Our work thus paves the way for the development of ultrafast quantum information processing at room temperature with molecular vibrations in a range of frequencies that has yet to be developed for optical quantum technology.

ACKNOWLEDGMENTS

J.F.T. was supported by ANID through the Postdoctoral Fellowship, Grant No. 3200565. F.H. was funded by ANID—Fondecyt Regular Grant No. 1181743. F.H. and A.D. also acknowledge support by ANID—and Millennium Science Initiative Program ICN17-012. A.D. was supported by ANID—Fondecyt Regular Grant No. 1180558, and M.A. was supported by ANID through the scholarship program Doctorado Becas Chile/2018—21181591. J.N., S.C.J., R.W., and M.B.R. acknowledge support from the Air Force Office of Scientific Research (AFOSR), Grant No. FA9550-21-1-0272. The Advanced Light Source (ALS) is supported by the Director, Office of Science, Office of Basic Energy Sciences, US Department of Energy, under Contract No. DE-AC02-05CH11231.

AUTHOR DECLARATIONS

Conflict of Interest

The authors have no conflicts to disclose.

DATA AVAILABILITY

The data that support the findings of this study are available from the corresponding author upon reasonable request.

APPENDIX A: CALIBRATION OF THE LINDBLAD MASTER EQUATION

The reduced density matrix of the coupled light-matter system $\hat{\rho}_S(t)$ evolves according to the quantum master equation in the Lindblad form,

$$\frac{d}{dt}\hat{\rho}_S = -i[\hat{\mathcal{H}}_N + \hat{H}_F(t), \hat{\rho}_S] + \mathcal{L}_\kappa[\hat{\rho}_S] + \mathcal{L}_{\gamma_C}[\hat{\rho}_S] + \mathcal{L}_{\gamma_L}[\hat{\rho}_S], \quad (A1)$$

where the undriven system Hamiltonian $\hat{\mathcal{H}}_N$ is given by Eq. (3) and the dissipators are given by⁸³

TABLE I. Measured resonator linewidth $\kappa/2\pi$ and vibrational dephasing time T_{2y}^{exp} for several resonance frequencies ω_c . The last two columns show the predicted Rabi coupling strengths and vibrational dephasing times.

ω_a (cm ⁻¹)	$\kappa/2\pi$ (cm ⁻¹)	T_{2y}^{exp} (fs)	$\sqrt{N}g$ (cm ⁻¹)	T_{2y} (fs)
1510	439.55	487.6 ± 52.9	30.5	488.6
1567	462.15	463.8 ± 29.5	31.0	464.1
1634	486.69	421.0 ± 20.9	32.5	423.8
1722	516.02	345.4 ± 10.3	40.2	346.8
1807	541.64	345.0 ± 8.2	41.5	338.0
1892	564.96	333.0 ± 9.2	49.0	336.1
1994	590.32	349.6 ± 13.2	54.0	349.1
2138	622.00	372.8 ± 18.9	59.7	374.8
2280	649.32	404.2 ± 23.6	63.5	404.7

$$\mathcal{L}_\kappa[\hat{\rho}] = \frac{\kappa}{2} (2 \hat{a} \hat{\rho} \hat{a}^\dagger - \hat{a}^\dagger \hat{a} \hat{\rho} - \hat{\rho} \hat{a}^\dagger \hat{a}), \quad (A2)$$

$$\mathcal{L}_{\gamma_C}[\hat{\rho}] = \frac{N\gamma_C}{2} (2 \hat{B}_0 \hat{\rho} \hat{B}_0^\dagger - \hat{B}_0^\dagger \hat{B}_0 \hat{\rho} - \hat{\rho} \hat{B}_0^\dagger \hat{B}_0), \quad (A3)$$

$$\mathcal{L}_{\gamma_L}[\hat{\rho}] = \frac{\gamma_L}{2} \sum_{i=1}^N (2 \hat{b}_i \hat{\rho} \hat{b}_i^\dagger - \hat{b}_i^\dagger \hat{b}_i \hat{\rho} - \hat{\rho} \hat{b}_i^\dagger \hat{b}_i). \quad (A4)$$

κ is the resonator field decay rate, $\gamma_N \equiv N\gamma_C$ is the vibrational relaxation rate into a collective reservoir (spontaneous emission and intermolecular phonon mode), and γ_L is the vibrational relaxation rate into a local reservoir (IVR).

We parameterize the quantum master equation in a two-step process: (1) We fix the frequencies and linewidths of the bare resonator and vibrational resonances from independent measurements taken in the absence of light-matter coupling. The infrared absorption linewidth in free space $\tilde{\gamma} \equiv \gamma/2\pi$ cm⁻¹ (FWHM) gives the bare dephasing time $T_{2y}^0 = 2/\tilde{\gamma}$. The width of the antenna resonance $\tilde{\kappa} = \kappa/2\pi$ cm⁻¹ gives the bare photon dephasing time $T_{2y}^0 = 2/\tilde{\kappa}$. (2) The free parameter $\sqrt{N}g$ is obtained by comparing the experimental decay time of the tail of the near-field interferogram, proportional to $\langle \hat{a}(t) \rangle$, with the simulated decay of $\langle \hat{B}_0(t) \rangle$. In Fig. 2(a), we fit the experimental FID decays to the exponential $\exp[-t/T_{2y}]$. We repeat this fitting procedure for a set of FID signals of the same resonator sample to get the experimental dephasing time T_{2y}^{exp} fs. The value of $\sqrt{N}g$ to be used in simulations is obtained by imposing the long-time decay time T_{2y} of $\langle \hat{B}_0(t) \rangle$ to match the decay time obtained by fitting the experimental FID trace. Table I shows the collective Rabi couplings that best reproduce the experimental dephasing times T_{2y} in Fig. 2(c) for several resonator frequencies ω_a close to the vibrational resonance $\omega_v = 1732$ cm⁻¹.

APPENDIX B: EXACT SOLUTIONS FOR $\langle \hat{a}(t) \rangle$ AND $\langle \hat{B}_0(t) \rangle$ UNDER A SINGLE GAUSSIAN PULSE

The mean field equations of motion in Eqs. (6) and (7) can be written in the form

$$\begin{pmatrix} y'_1(t) \\ y'_2(t) \end{pmatrix} = \begin{pmatrix} a_{11} & a_{12} \\ a_{21} & a_{22} \end{pmatrix} \begin{pmatrix} y_1(t) \\ y_2(t) \end{pmatrix} + \begin{pmatrix} f_1(t) \\ 0 \end{pmatrix} \quad (B1)$$

with $y_1 = \langle \hat{a} \rangle$, $y_2 = \langle \hat{B}_0 \rangle$, $a_{11} = -(\kappa/2 + i\omega_a)$, $a_{22} = -(\gamma/2 + i\omega_v)$, and $a_{12} = a_{21} = -ig_N$ with $g_N = \sqrt{N}g$. The initial condition is $(y_1, y_2)^T = 0$ at $t = 0$. The Gaussian driving function is given by

$$f_1(t) = -if_T \exp[-(t - t_0)^2/2T^2 - i\omega_d t], \quad (B2)$$

where $f_T = f_0/\sqrt{2\pi}T$ is the driving amplitude, T is the pulse width, and ω_d is the pulse carrier frequency. The pulse area is normalized. Solving for Eq. (B1) in the Laplace domain gives a vibrational coherence of the form

$$y_2(t) = \frac{a_{21}}{m_1 - m_2} \int_0^t f_1(\tau) (e^{m_1(t-\tau)} - e^{m_2(t-\tau)}) d\tau, \quad (B3)$$

where m_1 and m_2 are roots of the characteristic polynomial $p(s) = (s - a_{11})(s - a_{22}) - a_{12}a_{21}$, explicitly given by

$$m_{\pm} = \frac{1}{2}(a_{11} + a_{22}) \pm \frac{1}{2}\sqrt{(a_{11} - a_{22})^2 + 4a_{12}a_{21}} \quad (B4)$$

with the upper sign corresponding to m_1 . In terms of physical parameters, we have $m_j \equiv m'_j + im''_j = -(\gamma + \kappa)/4 - i(\omega_a + \omega_v)/2 \pm (\Gamma_g + i\Omega_g)/2$ with

$$\Gamma_g + i\Omega_g \equiv \sqrt{(i\Delta_a - \Delta_\Gamma)^2 - 4g_N^2}. \quad (B5)$$

The real quantities Γ_g and Ω_g modify the decay rates and oscillation frequencies of the coupled light-matter system, respectively. They depend on the detuning $\Delta_a = (\omega_a - \omega_v)$ and the decay mismatch $\Delta_\Gamma = (\gamma - \kappa)/2$.

Inserting Eq. (B2) in (B3) and evaluating the Gaussian integrals, we obtain

$$y_2(t) = -\left(\frac{f_0}{2}\right) \frac{g}{(\Gamma_g + i\Omega_g)} [e^{m_1 t} Q_1(t) - e^{m_2 t} Q_2(t)], \quad (B6)$$

where we introduced the envelope functions

$$Q_j(t) = e^{\frac{1}{2}k_j^2 T^2 + t_0 k_j} \left(\text{erf}\left[\frac{t - t_0 - k_j T^2}{\sqrt{2}T}\right] + \text{erf}\left[\frac{t_0 + k_j T^2}{\sqrt{2}T}\right] \right) \quad (B7)$$

with $k_j \equiv -m'_j - i(\omega_d + m''_j)$ and $\text{erf}(x)$ being the error function. The odd parity of the error function enforces $y_2(0) = 0$. Up to this point, the solution is exact. For a pulse kick ($T \rightarrow 0$) at $t = t_0$, the vibrational coherence in Eq. (B6) reduces to

$$y_2(t \gg t_0) \approx -\frac{g f_0}{\Gamma_g + i\Omega_g} e^{i\omega_d t_0} [e^{m_1(t-t_0)} - e^{m_2(t-t_0)}], \quad (B8)$$

determined only by the complex roots m_1 and m_2 , independent of the pulse duration T . For finite pulses, the dependence of the coherence on the pulse duration is given by the Q_j functions in Eq. (B7).

Solving now for the antenna coherence $y_1(t)$, we get

$$\begin{aligned} y_1(t) &= \frac{1}{a_{21}} \left(\frac{d}{dt} y_2(t) - a_{22} y_2(t) \right) \\ &= \left(\frac{if_0}{2} \right) \frac{1}{\Gamma_g + i\Omega_g} [(m_1 - a_{22}) e^{m_1 t} Q_1(t) \\ &\quad - (m_2 - a_{22}) e^{m_2 t} Q_2(t)] \\ &\quad - \left(\frac{if_0}{2} \right) \frac{1}{\Gamma_g + i\Omega_g} \left[e^{m_1 t} \frac{d}{dt} Q_1(t) - e^{m_2 t} \frac{d}{dt} Q_2(t) \right], \end{aligned} \quad (B9)$$

where in the first line we used $y_2(0) = 0$. The derivative envelope functions in the last line are given by

$$\frac{dQ_j(t)}{dt} = \frac{2}{\sqrt{2\pi}T} \exp\left[-\frac{(t - t_0)^2}{2T^2}\right] \exp[-m'_j + i(\omega_d - m''_j)], \quad (B10)$$

which are essentially replicas of the input Gaussian pulse [Eq. (B2)], modulated by an m_j -dependent exponential factor ($j = 1, 2$). For $t_0 \gg T$, the antenna coherence also satisfies $y_1(0) = 0$. In the limit of continuous driving ($T \rightarrow \infty$ with T/t_0 being a constant), the Q_j functions become independent of time for long times. The transient Gaussian-shape contribution to the antenna coherence thus vanishes, as expected.

Weak coupling solution: Under exact resonance ($\omega_a = \omega_v$) and large decay mismatch ($|\Delta_\Gamma| \gg 2g$), we have $\Omega_g \rightarrow 0$ in Eq. (B5). For $\kappa \gg \gamma$, we have $m_1 \approx -\tilde{\gamma}/2 - i\omega_v$ and $m_2 \approx -\tilde{\kappa}/2 - i\omega_a$ with coupled decay rates $\tilde{\gamma} \approx \gamma(1 + 4g_N^2/\kappa\gamma)$ and $\tilde{\kappa} \approx \kappa(1 - 4g_N^2/\kappa^2)$ (see also Ref. 62). For a pulse detuning from the resonator frequency $\Delta_d \equiv \omega_d - \omega_a$, the vibrational coherence can be written as

$$\begin{aligned} y_2(t) &= \frac{\sqrt{N}g f_0}{2\Gamma_g} e^{-i\omega_a t - i\Delta_d t_0} \left[e^{-\tilde{\gamma}(t-t_0)/2} Q_\gamma(t - t_\gamma) \right. \\ &\quad \left. - e^{-\tilde{\kappa}(t-t_0)/2} Q_\kappa(t - t_\kappa) \right], \end{aligned} \quad (B11)$$

where the timescales $t_\gamma \equiv t_0 + \tilde{\gamma}T^2/2$ and $t_\kappa \equiv t_0 + \tilde{\kappa}T^2/2$ can be written generally as t_α in the simplified envelope function

$$Q_\alpha(t - t_\alpha) \approx \left(1 + \text{erf}\left[\frac{t - t_\alpha}{\sqrt{2}T}\right] \right) e^{\frac{1}{2}(\tilde{\alpha}/2 - i\Delta_d)^2 T^2}. \quad (B12)$$

APPENDIX C: TIP-VIBRATION-RESONATOR SYSTEM

1. Coupled equations of motion

The dynamics considering dissipation can be treated with the Lindblad master equation in Eq. (4) of the main text with the system Hamiltonian given by Eqs. (10) and (11) plus by the tip dissipator,

$$\mathcal{L}_{\kappa_t}[\hat{\rho}_S] = (\kappa_t/2) (2\hat{c}\hat{\rho}_S\hat{c}^\dagger - \hat{c}^\dagger\hat{c}\hat{\rho}_S - \hat{\rho}_S\hat{c}^\dagger\hat{c}), \quad (C1)$$

where $\hat{\rho}_S$ is the total dipole-resonator-tip system density matrix and κ_t is the tip decay rate. From the Lindblad master equation, we obtain evolution equations for the resonator, dipole, and tip mean fields of the form

$$\begin{aligned} \frac{d}{dt} \langle \hat{a} \rangle &= -(\kappa_a/2 + i\omega_a) \langle \hat{a} \rangle - ig_{av} \langle \hat{B}_0 \rangle - ig_{at} \langle \hat{c} \rangle \\ &\quad - iF_1\phi_1(t) e^{-i(\omega_d t - \Delta\phi)}, \end{aligned} \quad (C2)$$

$$\frac{d}{dt} \langle \hat{B}_0 \rangle = -(\gamma/2 + i\omega_v) \langle \hat{B}_0 \rangle - ig_{av} \langle \hat{a} \rangle - ig_{vt} \langle \hat{c} \rangle, \quad (C3)$$

$$\begin{aligned} \frac{d}{dt}\langle\hat{c}\rangle &= -(\kappa_t/2 + i\omega_t)\langle\hat{c}\rangle - ig_{\text{at}}\langle\hat{a}\rangle - ig_{\text{vt}}\langle\hat{B}_0\rangle \\ &\quad - iF_2\phi_2(t)e^{-i\omega_c t}, \end{aligned} \quad (\text{C4})$$

where we have absorbed the \sqrt{N} -dependence of the tip-vibration and antenna-vibration couplings into g_{vt} and g_{av} , respectively. $\phi_i(t) = \exp[-(t - t_0)^2/2T_i^2]$ denotes a Gaussian pulse envelope.

2. Resonator response in the Fourier domain

Solving Eqs. (C2)–(C4) in the Fourier domain with $F_1\phi_1(\omega)e^{-i\omega_a t} = F_2\phi_2(\omega)e^{-i\omega_c t} = F(t)$, we obtain the following system of coupled differential equations:

$$M(\omega) \begin{pmatrix} \hat{a}(\omega) \\ \hat{b}(\omega) \\ \hat{c}(\omega) \end{pmatrix} = \begin{pmatrix} e^{i\Delta\phi} \\ 0 \\ 1 \end{pmatrix} F(\omega) \quad (\text{C5})$$

with

$$M(\omega) = \begin{pmatrix} 1/\chi_a(\omega) & -g_{\text{av}} & -g_{\text{at}} \\ -g_{\text{av}} & 1/\chi_v(\omega) & -g_{\text{vt}} \\ -g_{\text{at}} & -g_{\text{vt}} & 1/\chi_t(\omega) \end{pmatrix}. \quad (\text{C6})$$

By solving Eq. (C5) for the resonator field $\hat{a}(\omega) = \chi_T(\omega)F(\omega)$, we obtain an expression for the total field response function of the form

$$\chi_T(\omega) \equiv \chi_1(\omega) + \chi_2(\omega) + \chi_3(\omega) + \chi_4(\omega), \quad (\text{C7})$$

where

$$\chi_1(\omega) = D^{-1}(\omega)\chi_a(\omega)e^{i\Delta\phi}, \quad (\text{C8})$$

$$\chi_2(\omega) = -D^{-1}(\omega)g_{\text{vt}}^2\chi_v(\omega)\chi_t(\omega)\chi_a(\omega)e^{i\Delta\phi}, \quad (\text{C9})$$

$$\chi_3(\omega) = D^{-1}(\omega)g_{\text{at}}\chi_a(\omega)\chi_t(\omega), \quad (\text{C10})$$

$$\chi_4(\omega) = D^{-1}(\omega)g_{\text{av}}g_{\text{vt}}\chi_v(\omega)\chi_a(\omega)\chi_t(\omega) \quad (\text{C11})$$

with the bare response function given by

$$\chi_a(\omega) = (\omega - \omega_a - i\kappa_a/2)^{-1}, \quad (\text{C12})$$

$$\chi_v(\omega) = (\omega - \omega_v - i\gamma/2)^{-1}, \quad (\text{C13})$$

$$\chi_t(\omega) = (\omega - \omega_t - i\kappa_t/2)^{-1}, \quad (\text{C14})$$

and

$$\begin{aligned} D(\omega) &= 1 - g_{\text{av}}^2\chi_a(\omega)\chi_v(\omega) - g_{\text{vt}}^2\chi_t(\omega)\chi_v(\omega) \\ &\quad - g_{\text{at}}\chi_a(\omega)\chi_t(\omega)[g_{\text{at}} + 2g_{\text{av}}g_{\text{vt}}\chi_v(\omega)]. \end{aligned} \quad (\text{C15})$$

For $g_{\text{at}} = g_{\text{av}} = 0$, $\chi_T(\omega) = \chi_a(\omega)$ up to a global phase, regardless of g_{vt} . In this regime, the antenna resonator is only a spectator of the tip-vibration dynamics. On the other hand, when $g_{\text{vt}} = 0$ and $\phi_1 = \phi_2$, Eq. (C7) reduces to Eq. (12) of the main text.

To study the emergence of the Rabi sidebands in Fig. 4(b), we show in Fig. 6 the individual contributions to $\chi_T(\omega)$ under conditions of strong tip-vibration coupling $g_{\text{vt}} > \kappa \gg g_{\text{at}} \sim g_{\text{av}} \gg \gamma$,

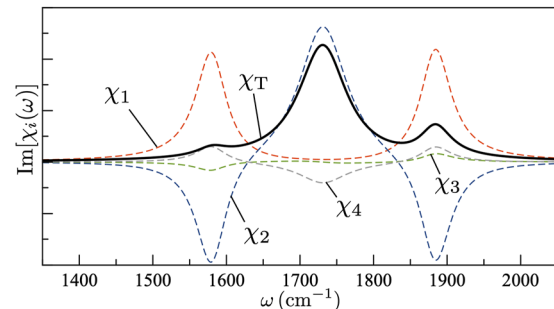


FIG. 6. Absorptive response ($\text{Im}[\chi_T(\omega)]$) of a fully resonant coupled antenna-vibration-tip system at the vibration frequency $\omega_v = 1730 \text{ cm}^{-1}$ (Black line). Dashed lines correspond to each term of the total antenna response function in Eq. (C7) with the relative tip-antenna phase $\Delta\phi = 0$ and $(\gamma/2\pi, \kappa_a/2\pi, \kappa_t/2\pi, \sqrt{N}g_{\text{av}}, g_{\text{at}}, g_{\text{vt}}) = (21, 80, 80, 23, 12, 150) \text{ cm}^{-1}$.

assuming a fully resonant scenario ($\omega_v = \omega_a = \omega_t$). In the Fano regime, we set $\kappa_t = \kappa_a = \kappa$, $\Delta\phi = 0$, and $g_{\text{av}} = 0$ ($\chi_4 = 0$) and evaluate the non-vanishing terms of $\text{Im}\chi_T(\omega)$ at $\omega = \omega_v \pm g_{\text{vt}}$ to obtain Eq. (17) in the main text.

3. Adiabatic elimination of the tip dynamics

Under the frequency hierarchy $\kappa_t \gg \kappa_a \gtrsim \gamma$, Eq. (C4) can be adiabatically eliminated from the system dynamics under steady state conditions to give effective evolution equations for the resonator and dipole coherences of the form

$$\begin{aligned} \frac{d}{dt}\langle\hat{a}\rangle &= -(\kappa'/2 + i\omega'_a)\langle\hat{a}\rangle - g'_{\text{av}}\langle\hat{B}_0\rangle + g'_{\text{at}}F_2\phi_2(t)e^{-i\omega_c t} \\ &\quad + \epsilon_d F_1\phi_1(t)e^{-i\omega_a t}, \end{aligned} \quad (\text{C16})$$

$$\frac{d}{dt}\langle\hat{B}_0\rangle = -(\gamma'/2 + i\omega'_v)\langle\hat{B}_0\rangle - g'_{\text{av}}\langle\hat{a}\rangle + g'_{\text{vt}}F_2\phi_2(t)e^{-i\omega_c t}, \quad (\text{C17})$$

which are analog to Eqs. (6) and (7) in the main text, except that the bare system frequencies and light-matter coupling constants are renormalized by the instantaneous tip amplitude as follows:

$$\kappa' = \kappa_a + \frac{4g_{\text{at}}^2/\kappa_t}{1 + 4Q_t^2}, \quad (\text{C18})$$

$$\tilde{\gamma} = \gamma + \frac{4g_{\text{vt}}^2/\kappa_t}{1 + 4Q_t^2}, \quad (\text{C19})$$

$$\omega'_a = \omega_a - \frac{4Q_t g_{\text{at}}^2/\kappa_t}{1 + 4Q_t^2}, \quad (\text{C20})$$

$$\omega'_v = \omega_v - \frac{4Q_t g_{\text{vt}}^2/\kappa_t}{1 + 4Q_t^2}, \quad (\text{C21})$$

$$g'_{\text{av}} = \frac{2g_{\text{vt}}g_{\text{at}}/\kappa_t}{1 + 4Q_t^2} + i\left(g_{\text{av}} - \frac{4Q_t g_{\text{vt}}g_{\text{at}}/\kappa_t}{1 + 4Q_t^2}\right), \quad (\text{C22})$$

$$\epsilon_d = -ie^{+i\Delta\phi}, \quad (\text{C23})$$

$$g'_{\text{at}} = -\frac{2g_{\text{at}}/\kappa_t}{1+4Q_t^2} + i\frac{4Q_t g_{\text{at}}/\kappa_t}{1+4Q_t^2}, \quad (\text{C24})$$

$$g'_{\text{vt}} = -\frac{2g_{\text{vt}}/\kappa_t}{1+4Q_t^2} + i\frac{4Q_t g_{\text{vt}}/\kappa_t}{1+4Q_t^2}, \quad (\text{C25})$$

where $Q_t = \omega_t/\kappa_t$ is the quality factor of the tip.

Solving Eqs. (C15) and (C16) for the Laplace transform of the resonator field $\langle \hat{a}(s) \rangle$ under vanishing initial conditions, we obtain

$$\langle \hat{a}(s) \rangle = \frac{(s - a_{22})}{p(s)} G_1(s, \Delta\phi) + \frac{a_{12}}{p(s)} G_2(s), \quad (\text{C26})$$

where $p(s) = (s - a_{11})(s - a_{22}) - a_{12}a_{21}$, $a_{11} = -\kappa'/2 - i\omega_c$, $a_{22} = -\gamma'/2 - i\omega'_v$, and $a_{12} = a_{21} = -g'_{\text{av}}$. The source terms are given by $G_1(s, \Delta\phi) = \tilde{g}_{\text{at}} F_2(s) - i e^{i\Delta\phi} F_1(s)$ and $G_2(s) = \tilde{g}_{\text{vt}} F_2(s)$ with $F_1(s) = \mathcal{L}[F_1 \phi_1(t) e^{-i\omega_c t}]$ and $F_2(s) = \mathcal{L}[F_2 \phi_2(t) e^{-i\omega_v t}]$ being the Laplace transforms of the pulse sources. For equal pulses [$F_1(s) = F_2(s) = F(s)$] and vanishing tip-dipole coupling ($g_{\text{vt}} \sim 0$), Eq. (C26) reduces to Eq. (15) in the main text.

APPENDIX D: ANHARMONIC VIBRATIONAL BLOCKADE

1. Exact finite-size calculations

The results in Figs. 5(b) and 5(c) were obtained by solving the Lindblad quantum master equation in Appendix A for a small collection of N molecules described by the stationary Hamiltonian

$$\hat{\mathcal{H}} = \omega_a \hat{a}^\dagger \hat{a} + \sum_{i=1}^N (\omega_v \hat{b}_i^\dagger \hat{b}_i - U \hat{b}_i^\dagger \hat{b}_i^\dagger \hat{b}_i \hat{b}_i) + g \sum_{i=1}^N (\hat{b}_i \hat{a}^\dagger + \hat{b}_i^\dagger \hat{a}), \quad (\text{D1})$$

where $U = \Delta_{21}/2$ gives the local anharmonic energy shift of higher vibrational levels. The total Hamiltonian includes the time-dependent driving term in Eq. (5), and for relaxation, we include local vibrational relaxation and photon decay with the Lindblad dissipators in Eqs. (A4) and (A2), respectively. The master equation is integrated numerically for small N by projecting the density matrix in the product basis $|v_i\rangle|n_c\rangle$, where $|v_i\rangle$ is a local vibrational eigenstate and $|n_c\rangle$ is a cavity Fock state. From the solution $\hat{\rho}(t)$, we obtain the collective vibrational coherence $\langle \hat{B}_0 \rangle = \sum_i \text{Tr}[\hat{b}_i \hat{\rho}(t)]/\sqrt{N}$ in Fig. 5(b) and other observables of interest.

To understand the degree of ground state depletion needed to obtain a nonlinear phase shift $\Delta\Phi_{\text{NL}} \sim 0.1\pi$, we solve the quantum master equation for a single molecule subject to a 155 fs pulse with strength $F_0 = 0.3\kappa$ and obtain the population of the lowest vibrational levels. The results are shown in Fig. 7. The ground state needs to be depleted by about 50% at the peak of the driving pulse to obtain $\Delta\Phi_{\text{NL}}/\pi \approx 0.1$. Despite this strong bleaching, the average photon number $\langle \hat{a}^\dagger \hat{a} \rangle$ remains low because photons leak out faster than they accumulate in the near-field ($F_0/\kappa < 1$). No significant population beyond $\nu = 3$ is found. The system parameters used in Fig. 7 are the same as in Fig. 5(b) (strong field response).

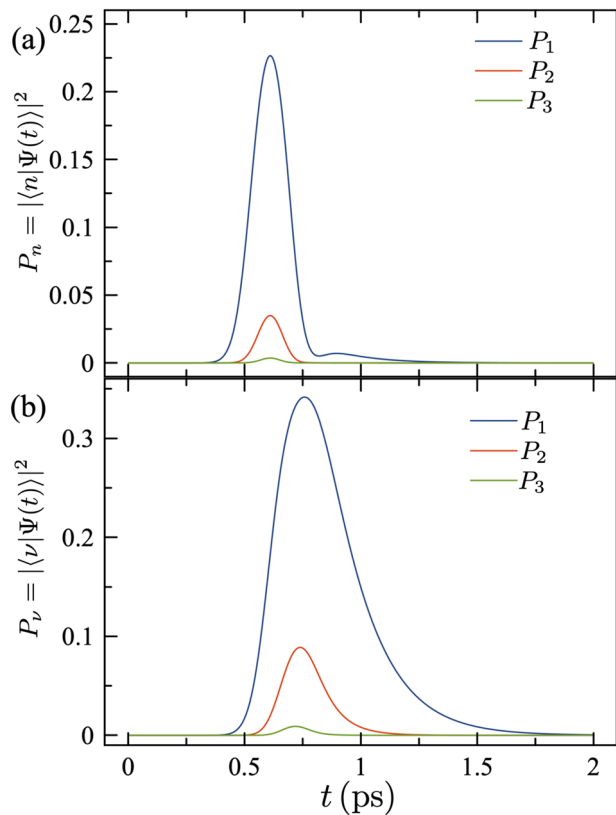


FIG. 7. Vibrational and Fock state population. (a) Evolution of the lowest cavity Fock states subject to a strong Gaussian pulse (FWHM = 155 fs) centered at 600 fs. (b) Vibrational population for the same driving pulse. System parameters are $(\gamma/2\pi, \kappa/2\pi, \sqrt{Ng}, U) = (17, 519, 41.5, 20) \text{ cm}^{-1}$ and $F_0/\kappa = 0.3$.

2. Vibrational chirping model

From the quantum master equation with the local anharmonic Hamiltonian in Eq. (D1), the equations of motion for the collective coherence are given by

$$\frac{d}{dt} \langle \hat{B}_0 \rangle = -(\gamma/2 + i\omega_v) \langle \hat{B}_0 \rangle - i\sqrt{Ng} \langle \hat{a} \rangle + i \frac{2U}{\sqrt{N}} \sum_{j=1}^N \langle \hat{b}_j^\dagger \hat{b}_j^\dagger \hat{b}_j \rangle, \quad (\text{D2})$$

where the cubic correlation results directly from the Kerr anharmonicity in the vibrational Hamiltonian. Solving for $\langle \hat{B}_0 \rangle$ and $\langle \hat{a} \rangle$ thus requires extending the evolution equations to include the dynamics of $\langle \hat{b}_j^\dagger \hat{b}_j^\dagger \hat{b}_j \rangle$ and linked observables, which forms a truncated hierarchy of coupled nonlinear equations that can be solved with standard methods.⁸⁷ Depending on the problem, the complexity of solving the hierarchy of coupled equations could be as high as numerically integrating the quantum master equation directly. Therefore, approximate solutions can be valuable to gain physical insights.

We can approximately close the hierarchy of equations at the mean field level by assuming that the states of the antenna (cavity) field and the vibrational ensemble are given by coherent states of the form

$$|\psi_{\text{ant}}(t)\rangle = e^{|\alpha(t)|^2/2} \sum_{n_c=0}^{\infty} \frac{\alpha(t)^{n_c}}{\sqrt{n_c!}} |n_c\rangle, \quad (\text{D3})$$

$$|\psi_N(t)\rangle = e^{|\beta(t)|^2/2} \sum_{k=0}^{\infty} \frac{\beta(t)^k}{\sqrt{k!}} |k\rangle_0. \quad (\text{D4})$$

Therefore, $|\psi_{\text{ant}}(t)\rangle$ is an eigenstate of \hat{a} with α being the eigenvalue and $|\psi_N(t)\rangle$ being an eigenstate of the collective operator \hat{B}_0 with eigenvalue β . The discrete index k denotes the total excitation level in the vibrational ensemble. Assuming only totally-symmetric configurations, the collective state with k excitations in an ensemble of N molecules is given by

$$|k\rangle_0 = \frac{1}{N^{k/2}} \sum_{v_1+\dots+v_N=k} \left[\frac{k!}{v_1! \dots v_N!} \right]^{1/2} |v_1, \dots, v_N\rangle, \quad (\text{D5})$$

where the summation runs over all the vibrational configurations that are consistent with the global excitation level k .

Inserting the wavefunction ansatz from Eqs. (D3) and (D4) into Eqs. (D2) and (6), we obtain the following closed system of coupled nonlinear equations for the coherent state amplitudes:

$$\frac{d}{dt} \alpha = -\left(\frac{\kappa}{2} + i\omega_c\right) \alpha - i\sqrt{N}g\beta - i\tilde{F}_d(t), \quad (\text{D6})$$

$$\frac{d}{dt} \beta = -\left(\frac{\gamma}{2} + i\left[\omega_v - \frac{2U|\beta|^2}{N}\right]\right) \beta - i\sqrt{N}g\alpha \quad (\text{D7})$$

from which the quadratic chirp term emerges. Promoting these scalar amplitudes to general mean field observables, i.e., $\alpha \rightarrow \langle \hat{a} \rangle$ and $\beta \rightarrow \langle \hat{B}_0 \rangle$, gives the vibrational chirping model in Eq. (19) discussed in the main text.

REFERENCES

1. S. Haroche, M. Brune, and J. M. Raimond, "From cavity to circuit quantum electrodynamics," *Nat. Phys.* **16**, 243–246 (2020).
2. R. J. Lewis-Swan, D. Barberena, J. A. Muniz, J. R. K. Cline, D. Young, J. K. Thompson, and A. M. Rey, "Protocol for precise field sensing in the optical domain with cold atoms in a cavity," *Phys. Rev. Lett.* **124**, 193602 (2020).
3. M. Reagor, W. Pfaff, C. Axline, R. W. Heeres, N. Ofek, K. Sliwa, E. Holland, C. Wang, B. Jacob, K. Chou, M. J. Hatridge, L. Frunzio, M. H. Devoret, L. Jiang, and R. J. Schoelkopf, "Quantum memory with millisecond coherence in circuit QED," *Phys. Rev. B* **94**, 014506 (2016).
4. S. Putz, D. O. Krimer, R. Amsüss, A. Valookaran, T. Nöbauer, J. Schmiedmayer, S. Rotter, and J. Majer, "Protecting a spin ensemble against decoherence in the strong-coupling regime of cavity QED," *Nat. Phys.* **10**, 720–724 (2014).
5. C. J. Hood, T. W. Lynn, A. C. Doherty, A. S. Parkins, and H. J. Kimble, "The atom-cavity microscope: Single atoms bound in orbit by single photons," *Science* **287**, 1447–1453 (2000).
6. P. W. H. Pinkse, T. Fischer, P. Maunz, and G. Rempe, "Trapping an atom with single photons," *Nature* **404**, 365–368 (2000).
7. J. D. Thompson, T. G. Tiecke, N. P. de Leon, J. Feist, A. V. Akimov, M. Gullans, A. S. Zibrov, V. Vuletić, and M. D. Lukin, "Coupling a single trapped atom to a nanoscale optical cavity," *Science* **340**, 1202–1205 (2013).
8. M. Lee, J. Kim, W. Seo, H.-G. Hong, Y. Song, R. R. Dasari, and K. An, "Three-dimensional imaging of cavity vacuum with single atoms localized by a nanohole array," *Nat. Commun.* **5**, 3441 (2014).
9. A. Reiserer and G. Rempe, "Cavity-based quantum networks with single atoms and optical photons," *Rev. Mod. Phys.* **87**, 1379–1418 (2015).
10. R. Chikkaraddy, B. de Nijs, F. Benz, S. J. Barrow, O. A. Scherman, E. Rosta, A. Demetriadou, P. Fox, O. Hess, and J. J. Baumberg, "Single-molecule strong coupling at room temperature in plasmonic nanocavities," *Nature* **535**, 127–130 (2016).
11. D. Wang, H. Kelkar, D. Martin-Cano, D. Rattenbacher, A. Shkarin, T. Utikal, S. Götzinger, and V. Sandoghdar, "Turning a molecule into a coherent two-level quantum system," *Nat. Phys.* **15**, 483–489 (2019).
12. Y.-S. Park, A. K. Cook, and H. Wang, "Cavity QED with diamond nanocrystals and silica microspheres," *Nano Lett.* **6**, 2075–2079 (2006).
13. W. L. Barnes, "Fluorescence near interfaces: The role of photonic mode density," *J. Mod. Opt.* **45**, 661–699 (1998).
14. C. Genes, D. Vitali, P. Tombesi, S. Gigan, and M. Aspelmeyer, "Ground-state cooling of a micromechanical oscillator: Comparing cold damping and cavity-assisted cooling schemes," *Phys. Rev. A* **77**, 033804 (2008).
15. K. W. Murch, U. Vool, D. Zhou, S. J. Weber, S. M. Girvin, and I. Siddiqi, "Cavity-assisted quantum bath engineering," *Phys. Rev. Lett.* **109**, 183602 (2012).
16. H. Cang, Y. Liu, Y. Wang, X. Yin, and X. Zhang, "Giant suppression of photobleaching for single molecule detection via the Purcell effect," *Nano Lett.* **13**, 5949–5953 (2013).
17. A. Shalabney, J. George, J. Hutchison, G. Pupillo, C. Genet, and T. W. Ebbesen, "Coherent coupling of molecular resonators with a microcavity mode," *Nat. Commun.* **6**, 5981 (2015).
18. J. P. Long and B. S. Simpkins, "Coherent coupling between a molecular vibration and Fabry-Perot optical cavity to give hybridized states in the strong coupling limit," *ACS Photonics* **2**, 130–136 (2015).
19. J. George, A. Shalabney, J. A. Hutchison, C. Genet, and T. W. Ebbesen, "Liquid-phase vibrational strong coupling," *J. Phys. Chem. Lett.* **6**, 1027–1031 (2015).
20. A. D. Dunkelberger, B. T. Spann, K. P. Fears, B. S. Simpkins, and J. C. Owrtusky, "Modified relaxation dynamics and coherent energy exchange in coupled vibration-cavity polaritons," *Nat. Commun.* **7**, 13504 (2016).
21. A. Shalabney, J. George, H. Hiura, J. A. Hutchison, C. Genet, P. Hellwig, and T. W. Ebbesen, "Enhanced Raman scattering from vibro-polariton hybrid states," *Angew. Chem., Int. Ed.* **54**, 7971–7975 (2015).
22. A. D. Dunkelberger, R. B. Davidson, W. Ahn, B. S. Simpkins, and J. C. Owrtusky, "Ultrafast transmission modulation and recovery via vibrational strong coupling," *J. Phys. Chem. A* **122**, 965–971 (2018).
23. B. Xiang, R. F. Ribeiro, Y. Li, A. D. Dunkelberger, B. B. Simpkins, J. Yuen-Zhou, and W. Xiong, "Manipulating optical nonlinearities of molecular polaritons by delocalization," *Sci. Adv.* **5**, eaax5196 (2019).
24. A. B. Grafton, A. D. Dunkelberger, B. S. Simpkins, J. F. Triana, F. J. Hernández, F. Herrera, and J. C. Owrtusky, "Excited-state vibration-polariton transitions and dynamics in nitroprusside," *Nat. Commun.* **12**, 214 (2021).
25. T. W. Ebbesen, "Hybrid light-matter states in a molecular and material science perspective," *Acc. Chem. Res.* **49**, 2403–2412 (2016).
26. J. Lather and J. George, "Improving enzyme catalytic efficiency by co-operative vibrational strong coupling of water," *J. Phys. Chem. Lett.* **12**, 379–384 (2021).
27. A. Kadyan, A. Shaji, and J. George, "Boosting self-interaction of molecular vibrations under ultrastrong coupling condition," *J. Phys. Chem. Lett.* **12**, 4313–4318 (2021).
28. M. V. Imperatore, J. B. Asbury, and N. C. Giebink, "Reproducibility of cavity-enhanced chemical reaction rates in the vibrational strong coupling regime," *J. Chem. Phys.* **154**, 191103 (2021).
29. R. M. A. Vergauwe, A. Thomas, K. Nagarajan, A. Shalabney, J. George, T. Chervy, M. Seidel, E. Devaux, V. Torbeev, and T. W. Ebbesen, "Modification of enzyme activity by vibrational strong coupling of water," *Angew. Chem., Int. Ed.* **58**, 15324–15328 (2019).
30. J. Lather, P. Bhatt, A. Thomas, T. W. Ebbesen, and J. George, "Cavity catalysis by cooperative vibrational strong coupling of reactant and solvent molecules," *Angew. Chem., Int. Ed.* **58**, 10635–10638 (2019).
31. K. Hirai, R. Takeda, J. A. Hutchison, and H. Uji-i, "Modulation of Prins cyclization by vibrational strong coupling," *Angew. Chem., Int. Ed.* **59**, 5332–5335 (2020).
32. F. Herrera and J. Owrtusky, "Molecular polaritons for controlling chemistry with quantum optics," *J. Chem. Phys.* **152**, 100902 (2020).
33. E. A. Muller, B. Pollard, H. A. Bechtel, R. Adato, D. Etezadi, H. Altug, and M. B. Raschke, "Nanoimaging and control of molecular vibrations through electromagnetically induced scattering reaching the strong coupling regime," *ACS Photonics* **5**, 3594–3600 (2018).

- ³⁴B. Metzger, E. Muller, J. Nishida, B. Pollard, M. Hentschel, and M. B. Raschke, "Purcell-enhanced spontaneous emission of molecular vibrations," *Phys. Rev. Lett.* **123**, 153001 (2019).
- ³⁵M. Autore, P. Li, I. Dolado, F. J. Alfar-Mozaz, R. Esteban, A. Atxabal, F. Casanova, L. E. Hueso, P. Alonso-González, J. Aizpurua, A. Y. Nikitin, S. Vélez, and R. Hillenbrand, "Boron nitride nanoresonators for phonon-enhanced molecular vibrational spectroscopy at the strong coupling limit," *Light: Sci. Appl.* **7**, 17172 (2018).
- ³⁶K. S. Menghrajani, H. A. Fernandez, G. R. Nash, and W. L. Barnes, "Hybridization of multiple vibrational modes via strong coupling using confined light fields," *Adv. Opt. Mater.* **7**, 1900403 (2019).
- ³⁷S. A. Mann, N. Nookala, S. C. Johnson, M. Cotrufo, A. Mekawy, J. F. Klem, I. Brener, M. B. Raschke, A. Alù, and M. A. Belkin, "Ultrafast optical switching and power limiting in intersubband polaritonic metasurfaces," *Optica* **8**, 606–613 (2021).
- ³⁸D. G. Baranov, M. Wersäll, J. Cuadra, T. J. Antosiewicz, and T. Shegai, "Novel nanostructures and materials for strong light-matter interactions," *ACS Photonics* **5**, 24–42 (2018).
- ³⁹J. Wang, K. Yu, Y. Yang, G. V. Hartland, J. E. Sader, and G. P. Wang, "Strong vibrational coupling in room temperature plasmonic resonators," *Nat. Commun.* **10**, 1527 (2019).
- ⁴⁰R. J. Koch, Th. Seyller, and J. A. Schaefer, "Strong phonon-plasmon coupled modes in the graphene/silicon carbide heterosystem," *Phys. Rev. B* **82**, 201413 (2010).
- ⁴¹I. J. Luxmoore, C. H. Gan, P. Q. Liu, F. Valmorra, P. Li, J. Faist, and G. R. Nash, "Strong coupling in the far-infrared between graphene plasmons and the surface optical phonons of silicon dioxide," *ACS Photonics* **1**, 1151–1155 (2014).
- ⁴²A. D. Dunkelberger, C. T. Ellis, D. C. Ratchford, A. J. Giles, M. Kim, C. S. Kim, B. T. Spann, I. Vurgaftman, J. G. Tischler, J. P. Long, O. J. Glembocki, J. C. Owrutsky, and J. D. Caldwell, "Active tuning of surface phonon polariton resonances via carrier photoionization," *Nat. Photonics* **12**, 50–56 (2018).
- ⁴³M. Autore, I. Dolado, P. Li, R. Esteban, F. J. Alfar-Mozaz, A. Atxabal, S. Liu, J. H. Edgar, S. Vélez, F. Casanova, L. E. Hueso, J. Aizpurua, and R. Hillenbrand, "Enhanced light-matter interaction in 10B monoisotopic boron nitride infrared nanoresonators," *Adv. Opt. Mater.* **9**, 2001958 (2021).
- ⁴⁴S. A. Mann, N. Nookala, S. Johnson, M. Ahmed, J. F. Klem, I. Brener, M. Raschke, A. Andrea, and M. A. Belkin, "Ultrafast optical switching and power limiting in intersubband polaritonic metasurfaces," in *Conference on Lasers and Electro-Optics* (Optical Society of America, 2020), p. FTu4Q.7.
- ⁴⁵S. Buhmann and D. Welsch, "Dispersion forces in macroscopic quantum electrodynamics," *Prog. Quantum Electron.* **31**, 51–130 (2007).
- ⁴⁶M. S. Tame, K. R. McEnergy, S. K. Özdemir, J. Lee, S. A. Maier, and M. S. Kim, "Quantum plasmonics," *Nat. Phys.* **9**, 329–340 (2013).
- ⁴⁷M. K. Schmidt, R. Esteban, A. González-Tudela, G. Giedke, and J. Aizpurua, "Quantum mechanical description of Raman scattering from molecules in plasmonic cavities," *ACS Nano* **10**, 6291–6298 (2016).
- ⁴⁸A. González-Tudela and J. I. Cirac, "Quantum emitters in two-dimensional structured reservoirs in the nonperturbative regime," *Phys. Rev. Lett.* **119**, 143602 (2017).
- ⁴⁹A. Delga, J. Feist, J. Bravo-Abad, and F. J. García-Vidal, "Quantum emitters near a metal nanoparticle: Strong coupling and quenching," *Phys. Rev. Lett.* **112**, 253601 (2014).
- ⁵⁰T. Neuman, R. Esteban, G. Giedke, M. K. Schmidt, and J. Aizpurua, "Quantum description of surface-enhanced resonant Raman scattering within a hybrid-optomechanical model," *Phys. Rev. A* **100**, 043422 (2019).
- ⁵¹M. K. Svendsen, Y. Kurman, P. Schmidt, F. Koppens, I. Kaminer, and K. S. Thygesen, "Combining density functional theory with macroscopic QED for quantum light-matter interactions in 2D materials," *Nat. Commun.* **12**, 2778 (2021).
- ⁵²M. Kamandar Dezfouli and S. Hughes, "Quantum optics model of surface-enhanced Raman spectroscopy for arbitrarily shaped plasmonic resonators," *ACS Photonics* **4**, 1245–1256 (2017).
- ⁵³J. Feist, A. I. Fernández-Domínguez, and F. J. García-Vidal, "Macroscopic QED for quantum nanophotonics: Emitter-centered modes as a minimal basis for multiemitter problems," *Nanophotonics* **10**, 477–489 (2021).
- ⁵⁴D. E. Westmoreland, K. P. McClelland, K. A. Perez, J. C. Schwabacher, Z. Zhang, and E. A. Weiss, "Properties of quantum dots coupled to plasmons and optical cavities," *J. Chem. Phys.* **151**, 210901 (2019).
- ⁵⁵C. Schneider, M. M. Glazov, T. Korn, S. Höfling, and B. Urbaszek, "Two-dimensional semiconductors in the regime of strong light-matter coupling," *Nat. Commun.* **9**, 2695 (2018).
- ⁵⁶V. Savona, L. C. Andreani, P. Schwendimann, and A. Quattropani, "Quantum well excitons in semiconductor microcavities: Unified treatment of weak and strong coupling regimes," *Solid State Commun.* **93**, 733–739 (1995).
- ⁵⁷T. T. Tran, K. Bray, M. J. Ford, M. Toth, and I. Aharonovich, "Quantum emission from hexagonal boron nitride monolayers," *Nat. Nanotechnol.* **11**, 37–41 (2016).
- ⁵⁸P. Kirton, M. M. Roses, J. Keeling, and E. G. Dalla Torre, "Introduction to the Dicke model: From equilibrium to nonequilibrium, and vice versa," *Adv. Quantum Technol.* **2**, 1800043 (2019).
- ⁵⁹K. M. Birnbaum, A. Boca, R. Miller, A. D. Boozer, T. E. Northup, and H. J. Kimble, "Photon blockade in an optical cavity with one trapped atom," *Nature* **436**, 87–90 (2005).
- ⁶⁰P. Rabl, "Photon blockade effect in optomechanical systems," *Phys. Rev. Lett.* **107**, 063601 (2011).
- ⁶¹S. Das, A. Grankin, I. Iakoupor, E. Brion, J. Borregaard, R. Boddeda, I. Usmani, A. Ourjoumtsev, P. Grangier, and A. S. Sørensen, "Photonic controlled-phase gates through Rydberg blockade in optical cavities," *Phys. Rev. A* **93**, 040303 (2016).
- ⁶²D. Plankensteiner, C. Sommer, M. Reitz, H. Ritsch, and C. Genes, "Enhanced collective Purcell effect of coupled quantum emitter systems," *Phys. Rev. A* **99**, 043843 (2019).
- ⁶³H. P. Breuer and F. Petruccione, *The Theory of Open Quantum Systems* (Oxford University Press, 2002).
- ⁶⁴F. J. Hernández and F. Herrera, "Multi-level quantum Rabi model for anharmonic vibrational polaritons," *J. Chem. Phys.* **151**, 144116 (2019).
- ⁶⁵J. F. Triana, F. J. Hernández, and F. Herrera, "The shape of the electric dipole function determines the sub-picosecond dynamics of anharmonic vibrational polaritons," *J. Chem. Phys.* **152**, 234111 (2020).
- ⁶⁶L. Ermann, G. G. Carlo, A. D. Chepelianskii, and D. L. Shepelyansky, "Jaynes-Cummings model under monochromatic driving," *Phys. Rev. A* **102**, 033729 (2020).
- ⁶⁷B. Pollard, E. A. Muller, K. Hinrichs, and M. B. Raschke, "Vibrational nanospectroscopic imaging correlating structure with intermolecular coupling and dynamics," *Nat. Commun.* **5**, 3587 (2014).
- ⁶⁸J. L. O'Brien, A. Furusawa, and J. Vučković, "Photonic quantum technologies," *Nat. Photonics* **3**, 687–695 (2009).
- ⁶⁹M. Micic, N. Klymyshyn, Y. D. Suh, and H. P. Lu, "Finite element method simulation of the field distribution for AFM tip-enhanced surface-enhanced Raman scanning microscopy," *J. Phys. Chem. B* **107**, 1574–1584 (2003).
- ⁷⁰B. S. Simpkins, J. P. Long, O. J. Glembocki, J. Guo, J. D. Caldwell, and J. C. Owrutsky, "Pitch-dependent resonances and near-field coupling in infrared nanoantenna arrays," *Opt. Express* **20**, 27725–27739 (2012).
- ⁷¹K. D. Park, M. A. May, H. Leng, J. Wang, J. A. Kropp, T. Gougousi, M. Pelton, and M. B. Raschke, "Tip-enhanced strong coupling spectroscopy, imaging, and control of a single quantum emitter," *Sci. Adv.* **5**, eaav5931 (2019).
- ⁷²M. A. May, D. Fialkow, T. Wu, K. D. Park, H. Leng, J. A. Kropp, T. Gougousi, P. Lalanne, M. Pelton, and M. B. Raschke, "Nano-cavity QED with tunable nano-tip interaction," *Adv. Quantum Technol.* **3**, 1900087 (2020).
- ⁷³M. Napolitano, M. Koschorreck, B. Dubost, N. Behbood, R. J. Sewell, and M. W. Mitchell, "Interaction-based quantum metrology showing scaling beyond the Heisenberg limit," *Nature* **471**, 486–489 (2011).
- ⁷⁴A. Piryatinski, V. Chernyak, and S. Mukamel, "Two-dimensional correlation spectroscopies of localized vibrations," *Chem. Phys.* **266**, 311–322 (2001).
- ⁷⁵R. Venkatramani and S. Mukamel, "Correlated line broadening in multidimensional vibrational spectroscopy," *J. Chem. Phys.* **117**, 11089–11101 (2002).
- ⁷⁶P. Saurabh and S. Mukamel, "Two-dimensional infrared spectroscopy of vibrational polaritons of molecules in an optical cavity," *J. Chem. Phys.* **144**, 124115 (2016).

- ⁷⁷R. F. Ribeiro, A. D. Dunkelberger, B. Xiang, W. Xiong, B. S. Simpkins, J. C. Owrusky, and J. Yuen-Zhou, "Theory for nonlinear spectroscopy of vibrational polaritons," *J. Phys. Chem. Lett.* **9**, 3766–3771 (2018).
- ⁷⁸B. Xiang, R. F. Ribeiro, A. D. Dunkelberger, J. Wang, Y. Li, B. S. Simpkins, J. C. Owrusky, J. Yuen-Zhou, and W. Xiong, "Two-dimensional infrared spectroscopy of vibrational polaritons," *Proc. Natl. Acad. Sci. U. S. A.* **115**, 4845–4850 (2018).
- ⁷⁹X. Jin, A. Cerea, G. C. Messina, A. Rovere, R. Piccoli, F. De Donato, F. Palazon, A. Perucchi, P. Di Pietro, R. Morandotti, S. Lupi, F. De Angelis, M. Prato, A. Toma, and L. Razzari, "Reshaping the phonon energy landscape of nanocrystals inside a terahertz plasmonic nanocavity," *Nat. Commun.* **9**(1), 763 (2018).
- ⁸⁰E. B. Wilson, J. C. Decius, and P. C. Cross, *Molecular Vibrations: The Theory of Infrared and Raman Vibrational Spectra* (Courier Corporation, 1980).
- ⁸¹E. C. Fulmer, P. Mukherjee, A. T. Krummel, and M. T. Zanni, "A pulse sequence for directly measuring the anharmonicities of coupled vibrations: Two-quantum two-dimensional infrared spectroscopy," *J. Chem. Phys.* **120**, 8067–8078 (2004).
- ⁸²A. D. Dunkelberger, A. B. Grafton, I. Vurgaftman, Ö. O. Soykal, T. L. Reinecke, R. B. Davidson, B. S. Simpkins, and J. C. Owrusky, "Saturable absorption in solution-phase and cavity-coupled tungsten hexacarbonyl," *ACS Photonics* **6**, 2719 (2019).
- ⁸³S. Nathan, N. Lambert, F. Nori, and S. De Liberato, "Superradiance with local phase-breaking effects," *Phys. Rev. A* **96**, 023863 (2017).
- ⁸⁴J. A. Campos-Gonzalez-Angulo, R. F. Ribeiro, and J. Yuen-Zhou, "Generalization of the Tavis–Cummings model for multi-level anharmonic systems," *New J. Phys.* **23**(6), 063081 (2021).
- ⁸⁵O. Ávalos-Ovando, L. V. Besteiro, Z. Wang, and A. O. Govorov, "Temporal plasmonics: Fano and Rabi regimes in the time domain in metal nanostructures," *Nanophotonics* **9**, 3587–3595 (2020).
- ⁸⁶F. Huth, A. Chuvilin, M. Schnell, I. Amenabar, R. Krutokhrostov, S. Lopatin, and R. Hillenbrand, "Resonant antenna probes for tip-enhanced infrared near-field microscopy," *Nano Lett.* **13**, 1065–1072 (2013).
- ⁸⁷V. M. Axt and S. Mukamel, "Nonlinear optics of semiconductor and molecular nanostructures: A common perspective," *Rev. Mod. Phys.* **70**, 145–174 (1998).